

**HIGH PRECISION FORCE APPLICATION AND TEMPERATURE
RESISTANT PROBE NACELLES FOR SUPERSONIC EXHAUST
CHARACTERIZATION**

by

Aubrey J. McKelvy

A Thesis

Submitted to the Faculty of Purdue University

In Partial Fulfillment of the Requirements for the degree of

Master of Science in Aeronautics and Astronautics



School of Aeronautics and Astronautics

West Lafayette, Indiana

December 2021

THE PURDUE UNIVERSITY GRADUATE SCHOOL
STATEMENT OF COMMITTEE APPROVAL

Dr. Guillermo Paniagua-Perez, Co-Chair

School of Mechanical Engineering

Dr. James Braun, Co-Chair

School of Mechanical Engineering

Dr. Sally Bane

School of Aeronautics and Astronautics

Dr. Terrence Meyer

School of Mechanical Engineering

Approved by:

Dr. Gregory Blaisdell

To my love, Sushrut

ACKNOWLEDGMENTS

The most important acknowledgment I have to give is to my advisors, Guillermo Paniagua and James Braun; they pushed me to become so much better than I was, and, when I was ready to take on the challenge of this research, they offered me opportunity, support, and guidance. I would also like to thank Professor Terry Meyer, who provided valuable insight into the theory and operation of velocimetry techniques and allowed me the use of his test cell and the THOR test stand, and Francois Falempin, who provided motivation and funding for portions of this work as well as guidance for the design of aerodynamic bodies in highspeed flows. I would like to acknowledge Venkat Athmanathan, who provided critical assistance with test cell operations and keen advice throughout my work.

I could not have completed my work without the assistance, technical, experimental, and moral, of my colleagues at PETAL. I would like to especially thank Michael Butzen and Saunak Debnath, who each provided significant assistance with the experimental portions of my work. I also thank Swapnil Ingale, Lakshya Bhatnagar, and Hunter Nowak, who shared their considerable expertise to improve the mechanical aspects of my designs.

The strength I summoned to complete this work was drawn from the love and support given to me by my family. My parents, Michael and Wendy McKelvy have supported me and displayed virtues I think are rare in the world but necessary to succeed in challenges such as this; I owe all that I am to my attempts to emulate their strength of character, their utter competence, and their fierce determination. I must also thank my sister, Lexi, for providing (in addition to love and support) a next-day Amazon delivery of the hanging scale which was critical to my research.

Finally, I want to thank my partner, Sushrut Karmarkar, who motivated me to take on this challenge.

TABLE OF CONTENTS

LIST OF TABLES	6
LIST OF FIGURES	7
ABSTRACT	9
1. INTRODUCTION	10
1.1 Objectives	11
1.2 Methodology	12
Objective 1: Precise Load Application	12
Objective 2: Laser Optics Nacelle	12
1.3 Outline of Manuscript	13
2. PRECISE LOAD APPLICATION	14
2.1 Model	14
2.1.1 Formulation and Derivation	16
2.1.2 Model Validation	22
2.2 Implementation	29
2.2.1 THOR thrust stand	29
2.2.2 STARR torquemeter	34
2.3 Calibration	41
2.3.1 THOR thrust stand	41
3. LASER OPTICS NACELLE	50
3.1 Model	50
3.1.1 Estimation of Flow Conditions	50
3.1.2 1-D Heat Transfer Model	53
3.1.3 Parametric Analysis	56
3.2 Mechanical Design	60
3.2.1 Internal Optical Layout	60
3.2.2 External Nacelle (Probe Body)	61
3.3 Proof of Concept Prototype	65
4. CONCLUSIONS	68
REFERENCES	69

LIST OF TABLES

Table 1: Absolute uncertainties of calibration input parameters for the validation test.	26
Table 2: Sensitivity of calibration constants to different error sources.	27
Table 3: Results from the validation test	28
Table 4: Calibration results for THOR thrust stand.....	48
Table 5: Flow properties near probe faces using isentropic flow relations.	51
Table 6: Comparison of isentropic flow relations to CFD values (CFD listed parenthetically)...	52

LIST OF FIGURES

Figure 2-1: Diagram showing simple pulley model relevant variables.	15
Figure 2-2: Plot showing passive vs active tension for a stiff system.	18
Figure 2-3: Diagram of pulley configuration for axial load application.....	19
Figure 2-4: Plots showing the theoretical response of a representative pulley system.....	20
Figure 2-5: Plot showing the theoretical response of the calibration system.	21
Figure 2-6: Experimental rig for model validation	23
Figure 2-7: Data collected from the model validation test	24
Figure 2-8: Flow chart of data processing procedure for validation testing.	25
Figure 2-9: A picture of the calibration weights being weighed.	26
Figure 2-10: Calibration plot for the validation test.	28
Figure 2-11. THOR RDE assembly with loadcell circled in red and the thrust axis shown in black.	30
Figure 2-12: Diagram showing basic loads considered for THOR rigging structural analysis.	32
Figure 2-13: CAD rendering of the THOR calibration rigging	33
Figure 2-14. The calibration frame is coupled to the back side of the THOR thrust stand.	34
Figure 2-15. Diagram of PT-2 showing location of the torquemeter.	35
Figure 2-16. Diagram of the load-end pulley system.	36
Figure 2-17: CAD rendering of a conceptual modification to the THOR calibration rigging for torque application.....	37
Figure 2-18: A CAD rendering of the torquemeter calibration rigging.....	38
Figure 2-19: A detailed view of the cable organization within the gantry transit pulleys.	39
Figure 2-20: Figures showing the stress distribution for the torquemeter calibration anchor (top) and torque bar (bottom)	41
Figure 2-21: Calibration rigging mounted to THOR thrust stand.....	42
Figure 2-22: A picture of the load mounting fixture secured to the THOR inner body.	43
Figure 2-23: Raw and filtered data collected during the first calibration loading cycle.....	44
Figure 2-24: A picture of weights being added onto the THOR calibration rig.	45
Figure 2-25: Measured signal plotted vs effort for the THOR calibration.	46

Figure 2-26: Calibration plot for THOR thrust stand.	47
Figure 2-27: Experimental THOR thrust data plotted with respect to oxidizer mass flow rate. ..	49
Figure 3-1. Cross-sectional views of a pipe coil cooling jacket (left) and a conventional cooling jacket (right).	50
Figure 3-2: A diagram of relevant faces and flow phenomenon for the estimation of probe heat flux.	51
Figure 3-3: A diagram of the 1-D fluid element and its associated temperature profile.	53
Figure 3-4: Flow chart for the cooling analysis	56
Figure 3-5: Plots of temperature profiles for water coolant (left) and gaseous nitrogen coolant (right)	57
Figure 3-6: A plot of temperature profiles for a nitrogen cooling scheme at different heads	58
Figure 3-7: A plot of maximum wall temperature as it varies with sonic area and head pressure (left). And a plot of the variation in maximum internal temperature with cooling channel geometry (right).	59
Figure 3-8: A CAD rendering of a FLASH optical setup using THORLABS components.....	61
Figure 3-9: A CAD rendering of the full-scale optical probe with profile dimensions listed.	62
Figure 3-10: Mach contour slices from a 3D RANS CFD analysis performed on the probe geometry.	63
Figure 3-11: Cross section of the probe body showing the cooling channel geometry.	64
Figure 3-12: Diagram of open cycle coolant scheme.	64
Figure 3-13: A transparent view of the probe prototype.....	65
Figure 3-14: An image detailing the important mechanical aspects of the probe mid-section.....	66
Figure 3-15: A CAD rendering of the prototype probe and test stand.....	67

ABSTRACT

In this thesis a calibration procedure and probe design are developed towards the precise measurement of thrust and exhaust velocity in supersonic propulsion systems with hot exhausts. First, a portable, modular calibration stand with maximum loads above 400 pounds and traceable precision under 1% is developed. Traceably precise calibration weights are used with a dead-weight calibration scheme integrating a block and tackle pulley system for force multiplication. A pulley friction model and novel hysteresis analysis method is developed to account for transmission losses. Secondly, a novel probe allowing survivability of optical hardware for femtosecond laser activation and sensing of hydroxyl (FLASH) velocimetry in Mach 6, 1,700K flow is designed, and manufacturing and test plans of a prototype probe for use with femtosecond laser electronic excitation tagging (FLEET) velocimetry are detailed. Survivability is provided by an open cycle gaseous nitrogen cooling scheme integrated with a stainless-steel probe body. A parametric analysis of cooling performance is also presented with varying coolant pressure and channel geometry is performed using a 1-D heat transfer model.

1. INTRODUCTION

Supersonic nozzles are critical components of rotating detonation engines [1], scramjets [2], and rockets [3]. Despite the longstanding interest in the advancement of these systems [4] and their miniaturization [15], significant challenges remain to the precise measurement of thrust and exhaust velocity, which are valuable statistics for the characterization of flow properties and nozzle efficiency [5]. Cited precisions of experimental thrust measurements from rotating detonation engines (RDE's) range from 5 to 10 percent [6] [7] [8] [9], and, while there have been efforts to measure the velocity fields of RDE's [10] [11] [12], the attainable measurements are limited by optical access, component survivability in close proximity to high heat fluxes, and particle lag [13] [14] [15].

Thrust measurement techniques fall into three well defined methodologies [16]: scale force, momentum balance, and component performance stacking. Of these three, the scale force methodology, which involves the measuring of loads imparted on the engine frame by its exhaust, is most direct, least intrusive, and provides the lowest uncertainty. These advantages make scale force thrust measurement schemes a common choice for experimental engine test facilities, such as the turbine-integrated high-pressure optical RDE (THOR) test platform operated at Zucrow labs [17], which features a modular combustion chamber which would be prohibitive to the momentum balance and component stacking methodologies. Despite the long history of scale force thrust measurement, there is still a wide variability of architectures depending on engine size, facility constraints, and the number of force components measured [18]. Single component systems are categorized into on-axis systems, such as the University of Michigan's RDE thrust stand [19], which place the loadcell on the test articles main axis, and off-axis systems, such as THOR, which place the loadcell offset from this axis. Multicomponent systems are significantly more complex and share many design features with wind tunnel force measurement systems [20]. Calibration of these architectures is a critical step of the design process and operation to maintain low uncertainties, account for expected tare loads, and identify operational characteristics of the system. Thrust stands without in-place calibration systems are at risk of unquantified and variable uncertainties. A mobile calibration system that could apply loads at or beyond the expected thrust range of the engine would provide a great benefit to the quality of measurements produced by

these thrust stands while avoiding the need for a total redesign and allowing for smaller permanent footprints.

Femtosecond laser electronic excitation tagging (FLEET) velocimetry is a form of molecular tagging velocimetry (MTV) [21], which has been demonstrated at Purdue’s Zucrow labs [22] and utilizes the dissociation and recombination of nitrogen molecules to provide long-lived fluorescence for velocimetry. The tagging laser used for FLEET MTV will also dissociate water molecules and produce localized concentrations of hydroxyl radicals. Femtosecond laser activation and sensing of hydroxyl (FLASH) is a similar type of MTV, which produces these radicals with a tagging laser and then illuminates them with planar laser-induced fluorescence (PLIF) via a second “read” laser. This type of diagnostic technique is useful in reacting flows and combustion aided wind tunnels, which are likely to have appreciable concentrations of water molecules.

While the techniques mentioned above allow direct measurements to be made of the harsh environments present in high speed, high enthalpy flows, they are limited in the versatility of their excitation regions without the ability to place redirecting optics in the flow. FLEET has been applied to restrictive test geometries before [23], but only in low enthalpy flows. There are several facilities dedicated to the research of supersonic and hypersonic flows with very high enthalpies [24] [25], which would significantly inhibit or entirely prohibit the use of laser-based velocimetry techniques. Including the necessary optical components within these harsh environments would require the development of unique cooling schemes for optical components. There has been significant research and development of cooled pressure sensors [26] [27] [28], mostly utilizing water based cooling jackets, but no published research into the use of cooled optical components was found. The capabilities of laser-based optical diagnostics for high enthalpy flows could be widely expanded with the development of cooling techniques for optical components.

1.1 Objectives

The focus of this work is to provide improvements to diagnostic techniques used for nozzle characterization by addressing both needs mentioned above: the development of cooled optical components to allow versatile optical access in extreme high-enthalpy environments, and the development of a mobile high-load calibration system to characterize the tares and operational characteristics of engine thrust stands without in-place calibration systems.

- The first objective is to develop a force balance to apply precise and traceably accurate loads up to 400 pounds with a precision less than or equal to 1%, enabling the calibration of thrust stands to precisions better than the cited 5% for the expected thrust range.
- The second objective is to develop a cooled nacelle for optical components, such that laser velocimetry techniques can be performed within the core of high-temperature flow up to Mach 6 at total temps of 1700K.

1.2 Methodology

A methodology is designed to fulfill each of the objectives listed above. These methodologies are described here.

Objective 1: Precise Load Application

Traceably precise calibration weights will be used with a dead-weight calibration scheme which integrates a block and tackle pulley system for force multiplication. A pulley friction model will be developed to account for transmission losses. The analytical model of stiction within the system and a corresponding algorithm will be developed first and used to compute non-ideal mechanical advantage and attain precise and accurate load points for calibration. Second, rigging to host the pulley system and to support the application of precise loads up to 500 pounds will be designed for two different scenarios. Third, the propagation of uncertainties will be tracked and used to compute the achieved load precision of the system.

Objective 2: Laser Optics Nacelle

A novel probe allowing survivability of optical hardware for femtosecond laser activation and sensing of hydroxyl (FLASH) velocimetry using a cooling scheme integrated with a probe body will be designed. The aerodynamic and thermal flow properties are predicted first using shock relations and Prandtl-Meyer expansion. Second, a one-dimensional cooling model based on conduction and convection is developed and used to inform the selection of material, coolant, and channel geometry. Third, a probe body is designed and analyzed using a 3D Reynolds Averaged Navier Stokes solver. Finally, a prototype is designed.

1.3 Outline of Manuscript

The remainder of this document will detail each of the methodologies described above, report on the results, and provide a discussion of how well each objective was achieved.

Chapter 2 details the development of the calibration system. This includes a derivation of the pulley friction model used to compute the applied loads, a description and associated results of a model validation test, a design overview of the calibration system, and, finally, the results of the THOR calibration.

Chapter 3 details the design of the cooled probe body. Details of the cooling analysis will be given, followed by an overview of the design, and, finally, a description of a prototype design and test plan.

In the final chapter, the objectives and proposed methodologies are assessed and discussed and conclusions are given.

2. PRECISE LOAD APPLICATION

2.1 Model

This section details the model used to predict the load applied by the calibration system and the associated uncertainties. Previous work on the modeling of pulley systems has been conducted by Miyasaka et al [29] for the control of a cable-driven surgical robot. The authors identify three sources (excluding effort) which affect the force transmitted by a cable: cable hysteretic force, cable damping, and cable-pulley friction. The hysteretic force is a function of cable elongation and the rate of change of cable elongation; cable damping is purely a function of the rate of change of cable elongation; cable-pulley friction is a function of the cable tension, the number of pulleys, the wrap angle, and the cable velocity. Only static solutions are relevant for the calibration method, so the cable damping and the velocity dependent hysteresis are neglected. Friction can be modeled with Coulomb, viscous, stiction, and Stribeck terms [30]; Coulomb, viscous, and Stribeck friction are all velocity dependent and will be neglected.

Figure 2-1 shows the simple pulley which serves as the basis for the model. Effort (T_1) is applied to the free active side and results in tension in the fixed passive side (T_2). Stiction refers to the static friction present between the pulley, with radius R_o , and its axle, with radius R_i , and results in a tension decay phenomenon described by Peng et al. [31].

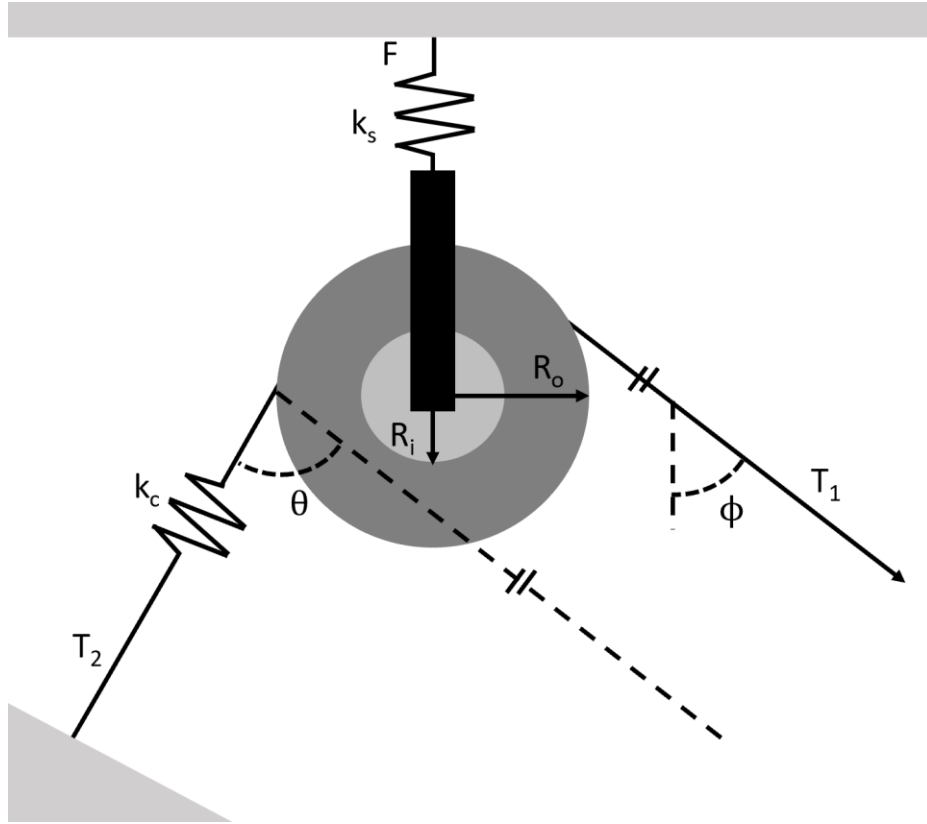


Figure 2-1: Diagram showing simple pulley model relevant variables.

The magnitude of stiction is related to the normal force acting on the axel, which is a function of T_1 , T_2 , and the wrap angle (θ). The pulley support is assumed to have linear elastic behavior and is modeled by a spring with stiffness k_s ; similarly, the cable hysteretic force is modeled by a spring in the passive cable with stiffness k_c . The same is neglected in the active cable because T_1 is independent of the hysteretic force. The following section will be focused on deriving an equation for the passive side tension as a function of the other variables in this system and then using this to build an expression for the static mechanical advantage provided by a generalized pulley system.

2.1.1 Formulation and Derivation

Peng et al. describe the tension decay with a transmission factor η , which relates the passive tension to the active tension such that

$$T_2 = \eta T_1 \quad (1)$$

The stiction and the tensions can be related by summing the moments around the pulley's central axis. For any static case, the pulley is at rest and the sum of moments is zero:

$$T_1 R_o - T_2 R_o - N \mu R_i = 0 \quad (2)$$

Here, μ is the coefficient of friction between the axel and pulley, and N is the normal force which can be expressed as

$$N = \sqrt{T_1^2 + 2 T_1 T_2 \cos(\theta) + T_2^2} \quad (3)$$

Combining equations (1), (2), and (3), gives the following expression for the transmission factor:

$$\eta = \frac{f + \cos\theta \pm \sqrt{2f(\cos\theta + 1) - \sin^2\theta}}{(f - 1)} \quad (4)$$

Where f is called the friction factor and is defined as

$$f = \frac{R_o^2}{R_i^2 \mu^2} \quad (5)$$

Equation (4) provides two sets of solutions; if the discriminant is taken as negative, this provides a transmission factor less than unity. This is the intuitive solution to the case described in Figure 2-1, with friction resisting the application of T_1 and reducing T_2 . A positive discriminant describes the second solution, where friction acts in the opposite direction; this would occur when the pulley is already under tension and T_1 is reduced.

The transmission factor is not strictly defined, as the coefficient of friction is variable within the bounds of the static coefficient of friction. The possible values for the transmission factor are

$$\eta^-(\mu_s) \leq \eta \leq \eta^+(\mu_s) \quad (6)$$

The plus and minus superscripts denote which discriminant is taken. Firmly defining the transmission factor for a stationary pulley requires accounting for the deflections of the fixed cable and of the system supporting the pulley. The force balance for the pulley is

$$F - T_1 \cos \phi + T_2 \cos(\theta - \phi) = 0 \quad (7)$$

In reference to any static loaded state, the deflections of the fixed cable (ΔL) and of the system (Δx) are related by

$$\Delta x = \Delta L \cos(\theta - \phi) \quad (8)$$

and allow a change in F to be related to a change in T_2 using Hooke's law:

$$\Delta F = \frac{k_s}{k_c} \Delta T_2 \cos(\theta - \phi) \quad (9)$$

Combining equations (7), (8), and (9) provides an expression for the change in T_2 with respect to change in T_1 for a non-rotating pulley (η'):

$$\eta' = \frac{\Delta T_2}{\Delta T_1} = \frac{\cos \phi}{\cos(\theta - \phi) \left(\frac{k_s}{k_c} - 1 \right)} \quad (10)$$

Equations (4) and (10) will be called the slip and non-slip transmission factors and fully describe a pseudo-static relationship between the passive and active tensions.

Figure 2-2 shows how the transmission factors affect the passive tension for an active tension that increases to 100 lbf then decreases back to zero with a $\frac{k_s}{k_c}$ much greater than unity and exaggerated friction coefficients. The dotted line represents a solution to both transmission factors, the red (outer) solid lines bound the transmission factor according to equation (6), and the blue (inner) solid lines represent the same equation evaluated at the kinetic friction coefficient. As the active tension increases, the passive tension changes with a slope equal to the non-slip transmission

factor until it reaches the outer solid line. At this point the static coefficient of friction is reached, and the pulley will slip. During the slip, the kinetic coefficient of friction applies and brings the pulley to rest along the inner solid line. The solution will bounce between the lower red and blue solid lines (defined by η^-) as active tension is increased; once the active tension begins reducing, the solution will follow the non-slip transmission factor until it reaches the upper red line (defined by η^+).

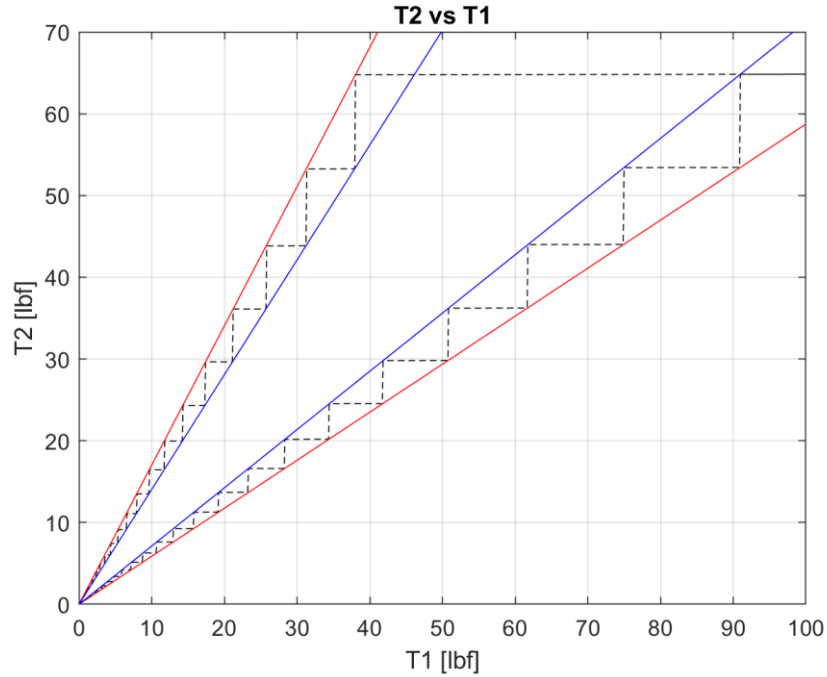


Figure 2-2: Plot showing passive vs active tension for a stiff system.

Mechanical advantage is provided by a pulley system because the effort is carried in the cable and supported twice by a single pulley. The pulley in Figure 2-1 provides a mechanical advantage of

$$MA = \frac{F}{T_1} = \cos\phi + \eta \cos(\theta - \phi) \quad (11)$$

Notice that the mechanical advantage is dependent on the transmission factor, so there will be a hysteresis like the behavior displayed in Figure 2-2. For a conventional block and tackle pulley system, the mechanical advantage is computed by summing the tensions falling from the moving

block, and the wrap angle is zero. Equation (11) can be generalized for this type of pulley system with

$$MA = \left[\prod_{i=1}^n \eta(f_i, \theta_i) \right] \sum_{j=0}^k \eta^j(f_j, \theta = 0) \cos(\phi_j) \quad (12)$$

where k is the number of pulleys in the block and tackle, n is the number of pulleys used to transmit the effort and load, and ϕ is the angle between a block and tackle cable and the loading axis. The “moving block” is the one that transmits the load, and the effort can be applied first to either the moving or fixed blocks. The above equation is configured for an effort connected to the moving block first. If the effort was connected to the fixed block, the index j should start at 1.

The behavior of the calibration system can be predicted using the previous set of equations. There are 6 pulleys in the most basic form of the calibration system; a diagram of the pulley configuration is shown in Figure 2-3. There are 2 pulleys used to transmit the effort (T_1) and 4 pulleys in a block and tackle configuration. The cable is terminated on the moving block, giving an ideal mechanical advantage of 5. The load (F) is measured with a load cell which is supporting the moving block.

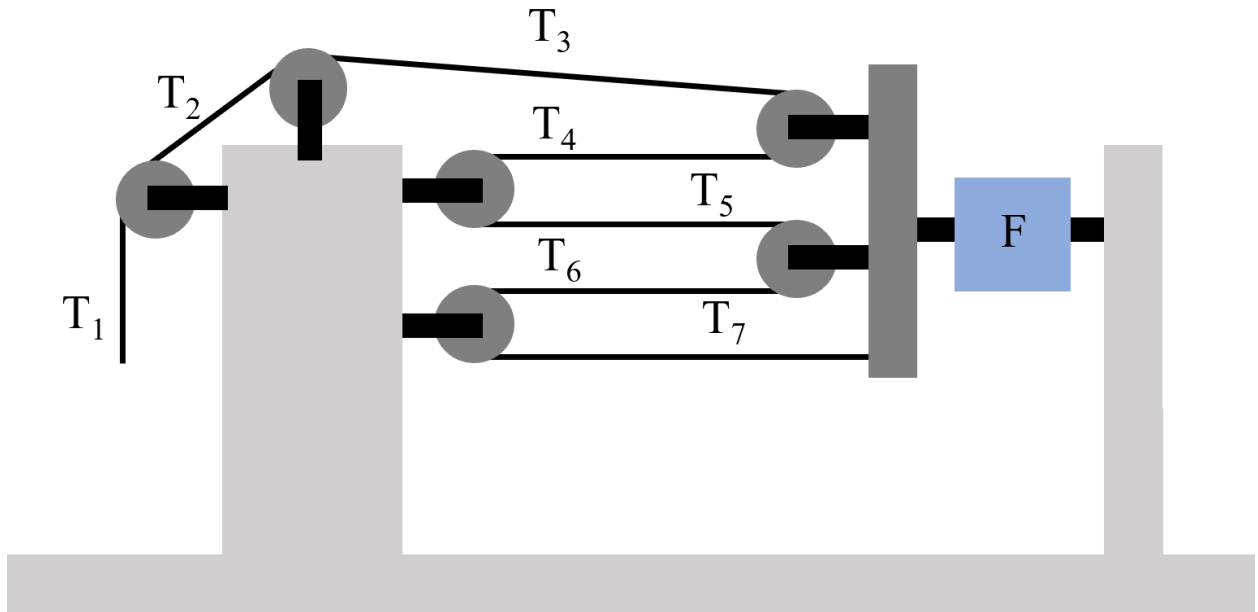


Figure 2-3: Diagram of pulley configuration for axial load application.

Equations (4) and (10) can be applied in the same process used to generate Figure 2-2 except here the passive tension computed for the first pulley is input as the active tension for the next and so on. The load is computed by summing tensions 3 through 7. Realistic friction coefficients for dry steel on steel are used, and the system is assumed to be very stiff in comparison to the cable. The results of this calculation are plotted in Figure 2-4. The left plot shows the load with respect to the effort, and the right figure shows how each of the tensions change with the effort. Equation (12) was not used for this plot because it does not allow individual tracking of tensions, and, as the plot of tension histories shows, the pulleys do not transition rotation directions simultaneously.

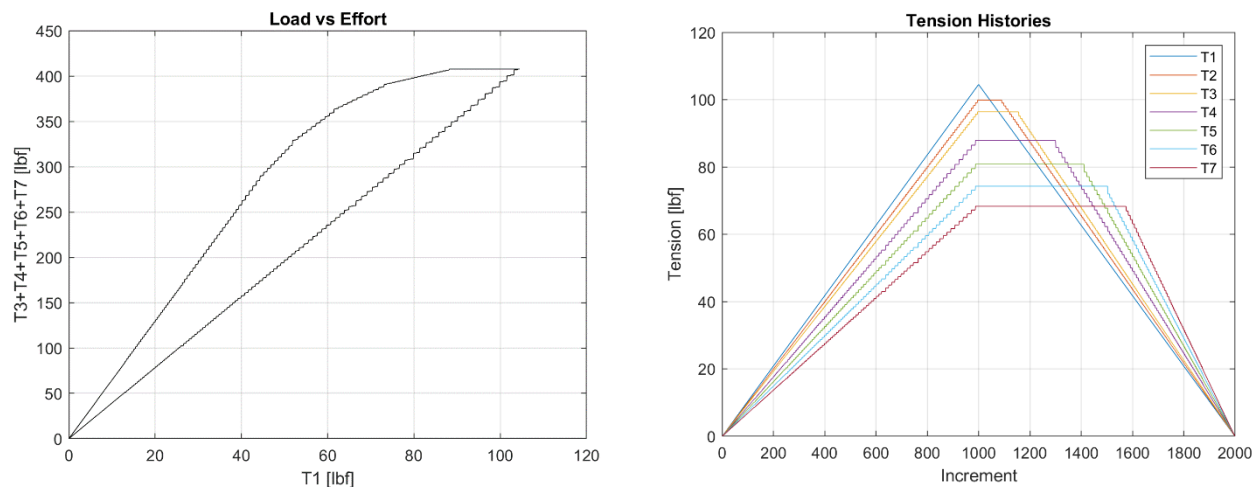


Figure 2-4: Plots showing the theoretical response of a representative pulley system.

Thus far, the behavior of pulley systems has been investigated for the case where the effort is very gradually incremented, allowing oscillation between solutions defined by kinetic and static friction. The calibration system will use weights of larger 10-pound increments. This has an advantageous effect: the pulleys will slip with every addition of weight, and almost every removal of weight. Figure 2-4 shows that it takes a reduction of more than 35 pounds from the max effort before all the pullies have fully transitioned. While loading, and after this point while unloading, all the pullies will slip together with each increment of effort, making the solutions in these regions well defined by equation (12) evaluated with the kinetic friction coefficient.

Figure 2-5 shows the same computation used to generate Figure 2-4 if modified to only include the addition and removal of 11 weights with the same maximum effort. This figure shows

what the experimental response to the calibration system is expected to be. The assumption that the system is much stiffer than the cable has the parameter $\frac{k_s}{k_c}$ set to 1000 and results in the tensions being nearly constant unless the pulley slips. When the first weight is removed from the maximum effort, there is effectively no change in load because of this assumption. If the stiffnesses are more similar, there will be a reduction in load regardless of slipping.

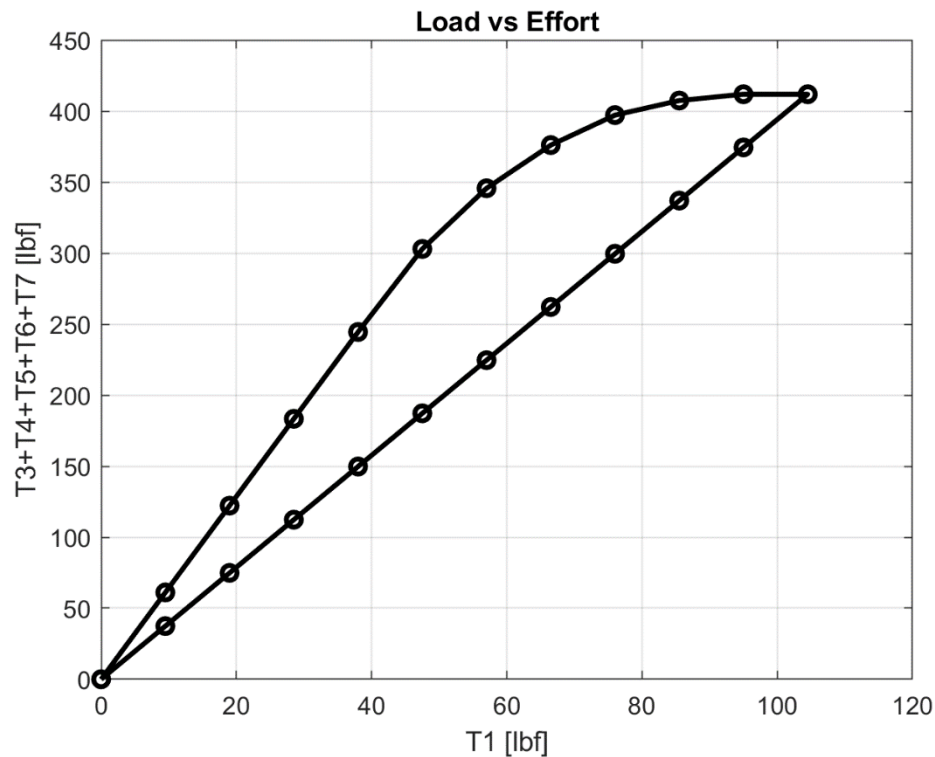


Figure 2-5: Plot showing the theoretical response of the calibration system.

If the calibration rigging is connected to some other system and data is collected, there will be two unknown parameters, the ratio of stiffnesses and the friction factor. The friction factor could be characterized for the pulley system beforehand but can also be computed from raw uncalibrated data. If it is assumed that each pulley has the same friction factor, then the ratio of fully slipped mechanical advantage during unloading vs mechanical advantage during loading is uniquely dependent on the friction factor:

$$\exists! f \frac{MA^+(f)}{MA^-(f)} \quad (13)$$

This function of f can be directly equated to uncalibrated data if the system response is linear. The calibration constants for a load measuring system take the form

$$V = mF + b \quad (14)$$

where V is the raw signal, typically in Volts, and m and b are the calibration constants. The offset b can be found trivially (by taking unloaded data) and subtracted, leaving voltage data that is directly proportional to load. If two different slopes of voltage with respect to effort are observed in the calibration due to the hysteresis discussed above, the ratio of these slopes is equal to the ratio of mechanical advantages shown in equation (13) because the calibration constant will cancel:

$$\frac{c^+ \frac{\Delta V}{\Delta T_1}}{c^- \frac{\Delta V}{\Delta T_1}} = \frac{c^+ \frac{m\Delta F}{\Delta T_1}}{c^- \frac{m\Delta F}{\Delta T_1}} = \frac{MA^+}{MA^-} \quad (15)$$

The ratio of mechanical advantages is equal to the ratio of slopes found in the uncalibrated signal for any system with a linear response. A similar process can be used to solve for the ratio of mechanical advantages for some non-linear responses but will not be detailed here. Once this value is computed from the raw data, a zero solver can be used with equation (12) to compute the friction factor. This is then input to the equation sets detailed above to provide tangible load values to use for calibration.

2.1.2 Model Validation

The model described in the previous section was validated using an experimental rig, shown in Figure 2-6, to host the same pulley system to be used in the calibration system and record load values. A simple frame is constructed from t-slotted framing rails and supports the fixed block and load from either end. The effort is provided by slotted weights placed on a high-hanger and supported by 7x19 patterned 5/32" wire rope. The tension in this cable is transmitted 90 degrees by two pulleys mounted on the frame before being routed through the block and tackle. The moving block applies the load and is connected to the frame through a RoMech Mini Crane Scale,

which provides load measurements. The whole assembly is placed on a table and clamped on the load end to prevent tipping from the effort. A set of control data was collected from the hanging scale by removing the pulley system and hanging the weights directly from the scale.



Figure 2-6: Experimental rig for model validation

The calibration process was mimicked, and the weights were loaded and then unloaded onto the validation test rigging. The load values recorded from the hanging scale are plotted in Figure 2-7. Data collected from this experiment agrees very well with the theoretical model, with the expected hysteresis present at similar proportions depicted in Figure 2-5, and features high repeatability. A key difference is the slope of points immediately following the unloading, with a decrease in load after the removal of the first weight, whereas the modeled load was constant. This indicates that the ratio of system to cable stiffness is not much greater than unity, as was assumed in the generation of Figure 2-5. This does not affect the slopes of the loading and unloading linear phases. The vertical axis of the plot is labeled “signal” because the hanging scale represents some uncalibrated loadcell; and it is expected that the calibration constants for this scale will be close to, but not exactly, unity.

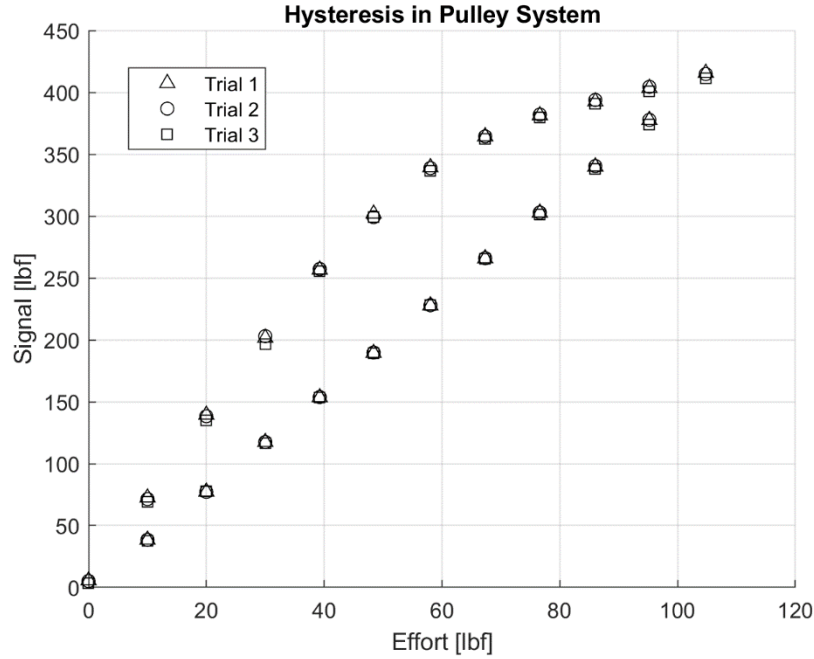


Figure 2-7: Data collected from the model validation test

The calibration method described in the previous section is employed by taking a least-squares fit of the entire loading curve (lower) and the last 5 points of the unloading curve (upper) where it is assumed all the pulleys have slipped. This process is repeated for each run in the data set, and the loading and unloading slopes are averaged. The friction factor corresponding to the two averaged slopes is computed using a zero solver with equations (12) and (13). The mechanical advantage of the linear portions of the loading and unloading curves is computed with this friction factor and multiplied by the effort to generate load data. Finally, this data is least-square fit with the corresponding signal values to generate calibration constants for the sensor. This process is shown as a flowchart in Figure 2-8.

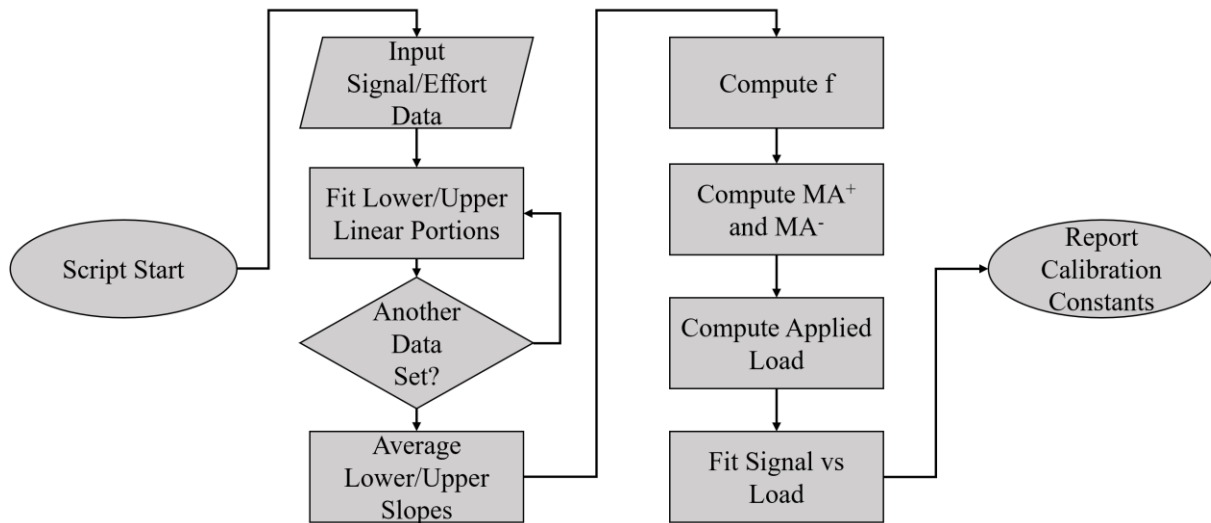


Figure 2-8: Flow chart of data processing procedure for validation testing.

Sources of uncertainty that must be propagated through the calibration method are shown in Table 1. The absolute uncertainties for the weights vary from 0.001 pounds to the maximum value shown in the table. The effort is created by a combination of purpose made slotted calibration weights and custom-made slotted weights. The uncertainty on the latter is limited by the scales used to weigh them. Stacking of the scale uncertainty was avoided by weighing each effort point independently on a Fairbanks Scales Model 70-2453-4, which provides uncertainties of 0.02 pounds up to 60 pounds, and of 0.05 for higher weights. Figure 2-9 shows the weighing of the highest effort point with the 8 custom weights stacked on top of the 3 purpose made weights. Each weight was labeled with a serial number to assure consistent placement order during the calibration. The three purpose made weights have a NIST traceable uncertainty of 0.001 pounds. The sensor uncertainty is estimated to be 2 pounds, despite the RoMech specifications listing much higher accuracy, based on drift observed in the digital readout during experimentation. The block and tackle cable angle uncertainty of 5 degrees is estimated based on the maximum angle that the cables can have if transiting from one pulley channel to the center of the opposing block with a pulley separation of 12 inches.



Figure 2-9: A picture of the calibration weights being weighed.

The high accuracy and NIST traceability of the purpose made slotted weights can be used to improve the uncertainty bounds and provide NIST traceability for the custom-made weights. A line is fit to the measurements from the Fairbanks scale for the purpose made weights with respect to their cited weights. This curve is used to correct the measured weights for every weight. This provides slightly lower uncertainty bounds for the custom-made weights.

Table 1: Absolute uncertainties of calibration input parameters for the validation test.

Source	Maximum Absolute Uncertainty
Weight [lb]	0.05
Sensor [lb]	2
Block and tackle cable angle [deg]	5

Whenever possible, uncertainties are propagated using the following equation for the uncertainty in a function of several variables [32]:

$$\delta q = \sqrt{\left(\frac{\partial q}{\partial x} \delta x\right)^2 + \dots + \left(\frac{\partial q}{\partial z} \delta z\right)^2} \quad (16)$$

There are some notable instances when this equation is impossible or impractical to apply: the first is the calculation of uncertainties in the friction factor, which does not have an analytical solution in terms of the ratio of mechanical advantages. The second is the calculation of uncertainty in the offset for linear regressions, which blows up for offsets near zero. For both cases, a min-max scheme is used, which evaluates the function with inputs at the minimum and maximum bounds of their uncertainty and takes the larger deviation in function value as the absolute uncertainty. This can be expressed as

$$\delta q \leq \max(|q(x, \dots, z) - q(x + \delta x, \dots, z + \delta z)|, |q(x, \dots, z) - q(x - \delta x, \dots, z - \delta z)|) \quad (17)$$

The sensitivity of the calibration constants to each of the error sources listed in Table 1 is given in Table 2. The sensitivities of the offset are deceptively large; this is, again, due to the very low mean value of the offset. The most impactful error source is the sensor uncertainty, which, per percent change in sensor values, produces a 25% change in slope and 13,000% change in offset.

Table 2: Sensitivity of calibration constants to different error sources.

Source	Sensitivity on m [%]	Sensitivity on b [%]
Weight	8.8	1,400
Sensor	25.0	13,000
Block and tackle cable angle	16.6	200

The results of the calibration procedure are shown in Figure 2-10. The black data points are the computed load values, and the blue points represent the control data collected by hanging the weights directly onto the scale. The red data points show values for the effort being multiplied by an ideal mechanical advantage which neglects friction. It is clear from the plot that the calibration method provides an improvement from the uncorrected data and that there is a strong agreement between the corrected values and the control values. A more detailed analysis of the control to corrected calibration is given below.

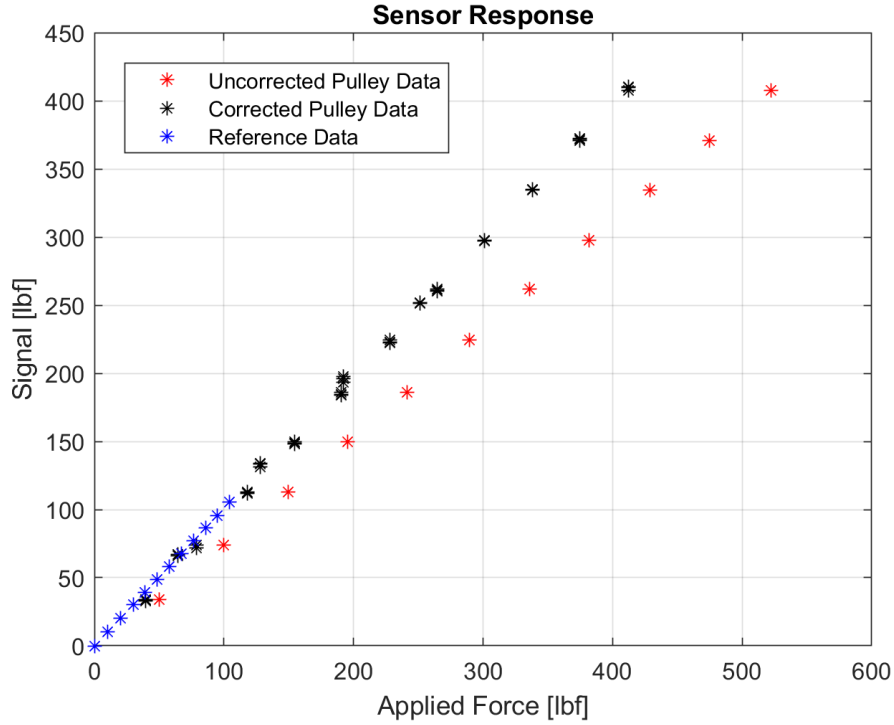


Figure 2-10: Calibration plot for the validation test.

The validation criteria for the calibration method are calibration constants that agree with those produced by the control data. Table 3 shows the calibration constants computed for the control and the corrected points along with R-square values. The corrected values do not provide a fit as linear as the control but does offer a lower uncertainty on the slope. This highlights the primary advantage of the calibration system, allowing a wider range of calibration points which allows lower uncertainties. Critically, the validation criteria are met, with the calibration constants, m and b , having insignificant discrepancy when compared to their error bounds.

Table 3: Results from the validation test

	m [lbf/lbf]	b [lbf]	R^2
Control	1.007 ± 0.013	0.0 ± 2	0.999997
Corrected	0.994 ± 0.004	-1.5 ± 2	0.999236

Unsurprisingly, the hanging scale has calibration scaling very near to 1, which is expected for a loadcell which is essentially pre-calibrated. However, the calibration does show that the hanging scale slightly underreports the load applied to it. The friction factor computed for the

pulley setup was 570 ± 50 . The pulleys in the block and tackle have an outer radius of 1.5” and an inner radius of 0.1407”. If a typical value for the kinetic friction coefficient of dry steel on steel of 0.42 is taken, this gives a theoretical friction factor of 644. The discrepancy is likely due to the two pulleys used for transmitting the tension before entering the block and tackle. These pulleys are smaller and have a theoretical friction factor of 142. Since every pulley in the system is assumed to have the same friction factor, the computed value will be some combination of the individual friction factors.

2.2 Implementation

This section will detail the design of rigging that enables the pulley system and calibration methodology detailed in the previous section to be applied to two different load measuring systems. The first is the THOR thrust stand [17], which incorporates a thrust table mounted on flexures that allow axial loads to be imparted on a pancake loadcell so that engine thrust can be measured. The second is the PETAL labs STARR turbine test rig [33], which couples test articles to a power dissipating motor via a rotary torquemeter to measure turbine torque.

2.2.1 THOR thrust stand

A CAD rendering of the THOR system is shown in Figure 2-11. The pancake loadcell is circled in red and placed under the thrust table and above the base. The flexures, which allow axial displacement of the thrust table, are visible to the right and left of the load cell. The RDE assembly is shown above the load cell and fixed to the thrust table by a truss structure. The engine exhaust velocity is to the right, creating thrust which pushes the thrust table to the left. Ideally the flexures provide no resistance to the axial displacement of the thrust table, leaving the entire load to be supported by the loadcell. The thrust table is coupled to the loadcell with a large bracket with a threaded rod; the loadcell is bolted onto the stand base via a similar bracket. The organization of this interface is such that the axial displacement of the thrust table is resisted by a tensile load through the loadcell.

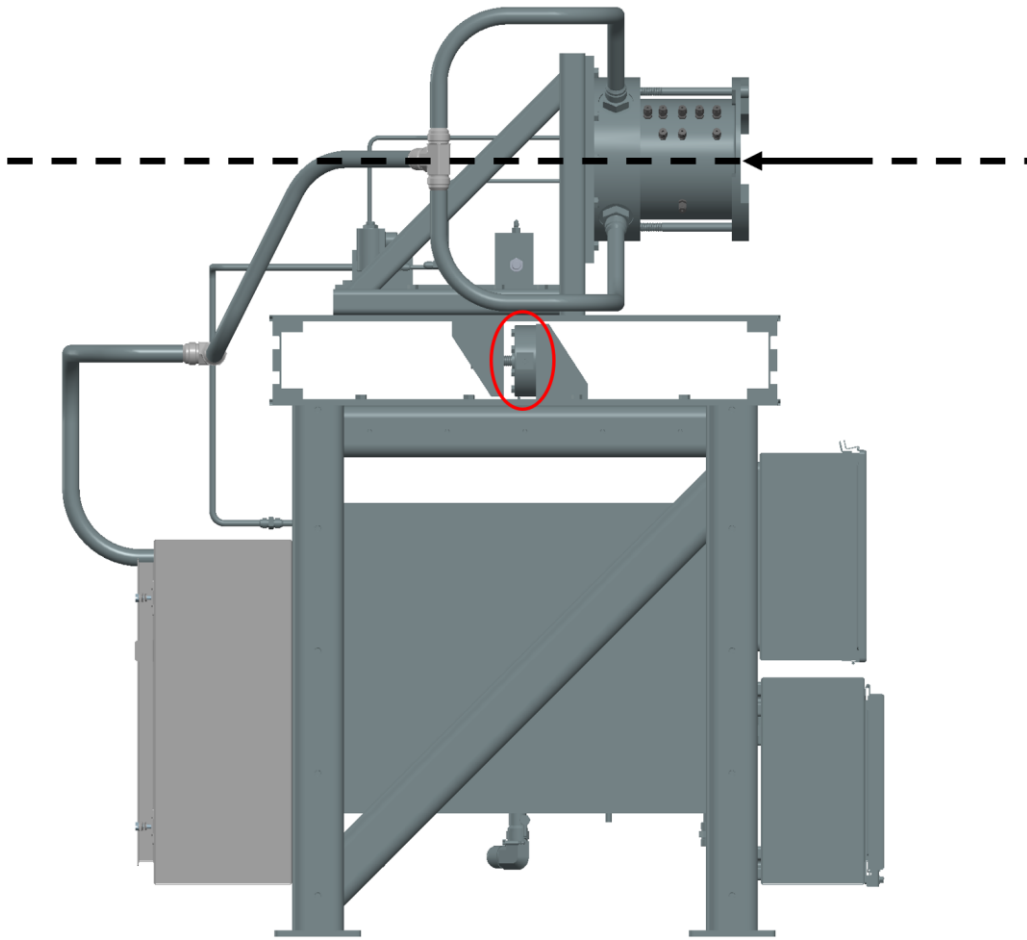


Figure 2-11. THOR RDE assembly with loadcell circled in red and the thrust axis shown in black.

Calibrating this loadcell for thrust produced by the RDE requires the calibration load to be applied along the central axis of the engine, shown as a black arrow in the figure. For the pulley system to apply loads along this axis, there must be a mounting fixture which places the fixed block in line with this axis and behind the engine. This will allow the moving block to be coupled to the engine and the tension between them to simulate loading conditions experienced during engine fires. The key requirement of the mounting fixture is to also be able to support the 500-pound calibration load.

Securing the mounting fixture requires coupling the rigging to some fixed surface or structure. There are two feasible choices for this, the test cell walls, floor, or gantry, or the thrust stand base. Each of these options has unique advantages and corresponding drawbacks. Using a

facility mounted rigging would allow hardpoints to be installed in the concrete test cell walls or floors which would provide support for the 500-pound load with minimal hardware and structural concerns. It would also allow the cables in the block and tackle to span very large distances, which would enable lower uncertainty in their angles and allow very large pulleys, which provide higher transmission factors. This type of fixture would also be much more obtrusive to test cell installations, requiring a cleared path along the thrust axis to the hardpoint, and would require more permanent modifications to the test cell in the form of wall or floor mounted hardpoints.

A mounting fixture secured to the thrust stand base would need to have similar dimensions to keep primary force transmitting members in line with the legs of the base. This would prohibit the precision advantages of long cables and large pullies but could be designed without permanent modifications to the test cell. Another key advantage to this type of fixture is flexibility and compartmentalization. This could be a module with variable dimensions to allow mounting with different thrust stands with minimal operational down time for engine testing. Analysis of the pulley friction model in the previous section shows that there is a relatively low sensitivity of uncertainty to deviation in cable angles, and stiction in the pulley system is suitably accounted for in the calculation of loads; for these reasons, the advantages of a facility mounted rigging do not outweigh the advantages of a base mounted rigging.

T-slotted 6105 aluminum framing is used for the structure for ease of construction and to allow resizing for integration with other thrust stands. Two large 3" posts are used as a backbone for the structure and transmit the primary load to the thrust stand base via one set of struts under compression and another set under tension. A diagram of these loads is shown in Figure 2-12. The upper set of struts is placed as high as possible while still able to abut the thrust stand base, and the lower struts are placed as low as possible. This minimizes the forces acting on them and minimizes the bending stress on the posts. The forces expected along each set of struts can be computed by equalizing their moments on the post with the calibration load. In a worse case, the upper struts will have to support 761 pounds of compressive loading, and the lower struts will have to support 261 pounds of tensile loading.

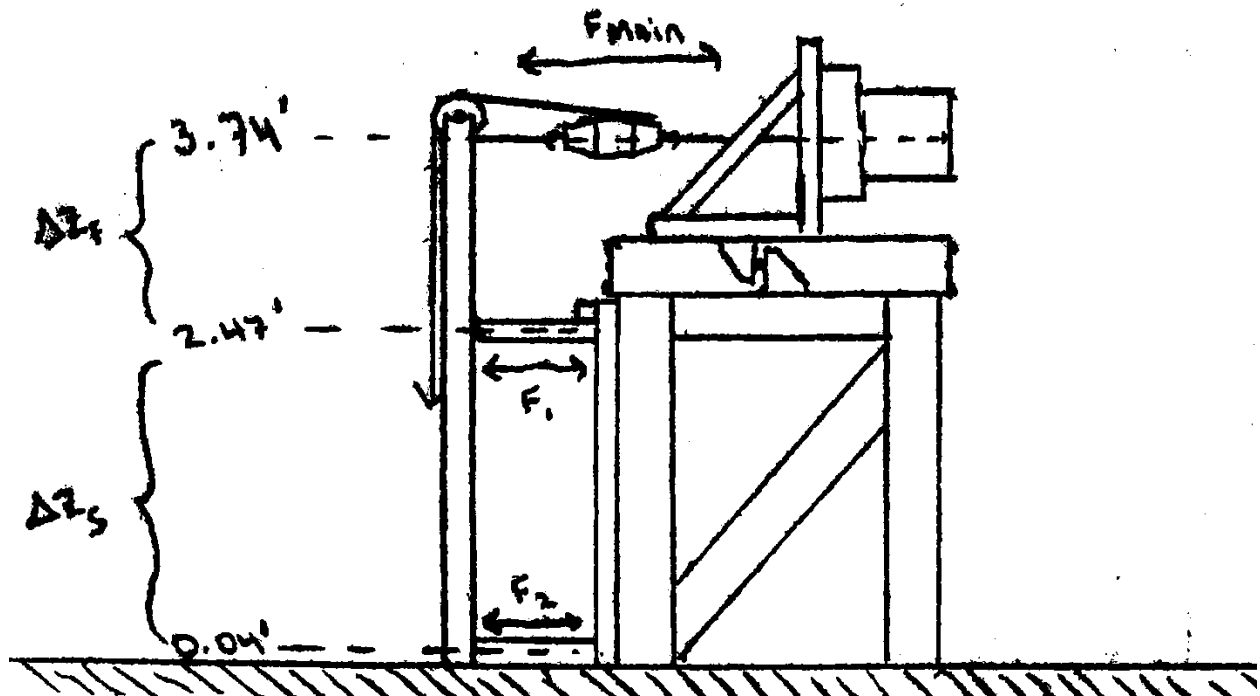


Figure 2-12: Diagram showing basic loads considered for THOR rigging structural analysis.

The compressive load on the upper members is split between two 1.5" t-slotted struts. These members have a cross-sectional area of 1.15 square inches, which gives a stress of 331 psi in each member. 6105 aluminum has a yield strength (CITE ASTM B221-21) of at least 17,000 psi which provides a factor of safety for the upper members greater than 50. The lower members are included primarily to provide upright alignment of the posts and rigidity to the structure; the tensile load will be supported two ratchet straps forming loops around each post and its corresponding thrust stand leg. With a cited capacity of 330 pounds and the looped configuration doubling this value, the factor of safety for these straps is 5. A simple computer aided bending analysis was done to confirm the structural integrity of the posts and of the rail which spans the posts and supports the load.

The construction of the calibration rigging is shown in Figure 2-13. The organization of the t-slotted framing allows the height of the upper and lower struts to be freely adjusted, as well as the width spanned by the struts and posts, while avoiding the use of brackets to support any of the primary loads. Components of the design, such as the truss members on the upper struts and

the mid and bottom section cross beams, were added to provide rigidity. The cross beams at the THOR side of the struts provide a contact surface for the thrust stand.

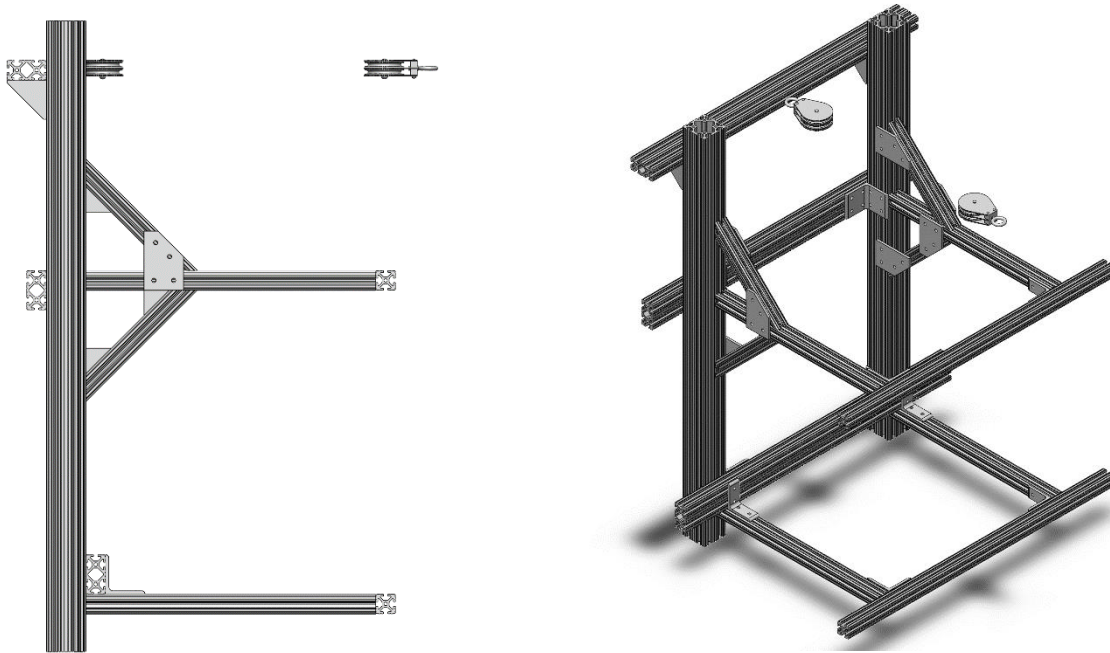


Figure 2-13: CAD rendering of the THOR calibration rigging

Mating of the calibration structure to THOR is achieved by using four ratchet straps in line with each strut. Figure 2-14 shows a CAD rendering of this structure mated with THOR.

A framework of 80/20 aluminum extrusions is coupled to the fixed portion of the thrust stand and hosts the pulleys. This framework, shown in Figure 2-14, is designed such that the mounting points can be moved horizontally and vertically to allow use with other horizontal thrust stands. The stationary block is mounted as far from the moving block as possible to minimize cosine losses.

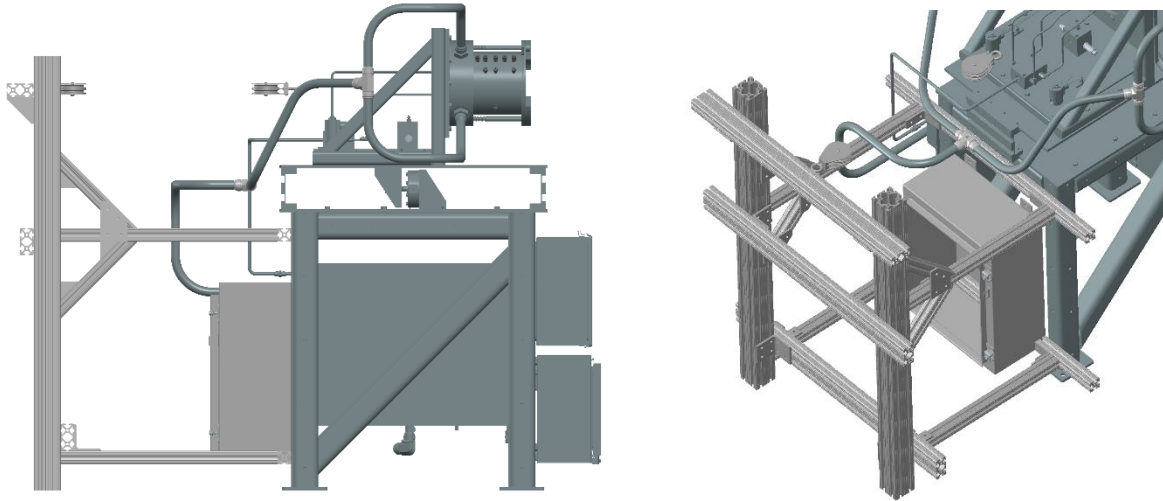


Figure 2-14. The calibration frame is coupled to the back side of the THOR thrust stand.

2.2.2 STARR torquemeter

The torquemeter used with the STARR turbine test rig is mounted axially within the PETAL PT-2 wind tunnel as shown in Figure 2-15. Calibration torques up to 350 foot-pounds are required; applying the 500-pound tension provided by the block and tackle as a torque requires the use of additional pulleys to reorganize and transmit the load. The load is split between two cables, which are routed to either end of a moment arm coupled to the torquemeter. Splitting the load between two cables places 250 pounds on each and requires a moment arm that is 16.8 inches long to give 350-foot pounds of torque at 500 pounds of load.

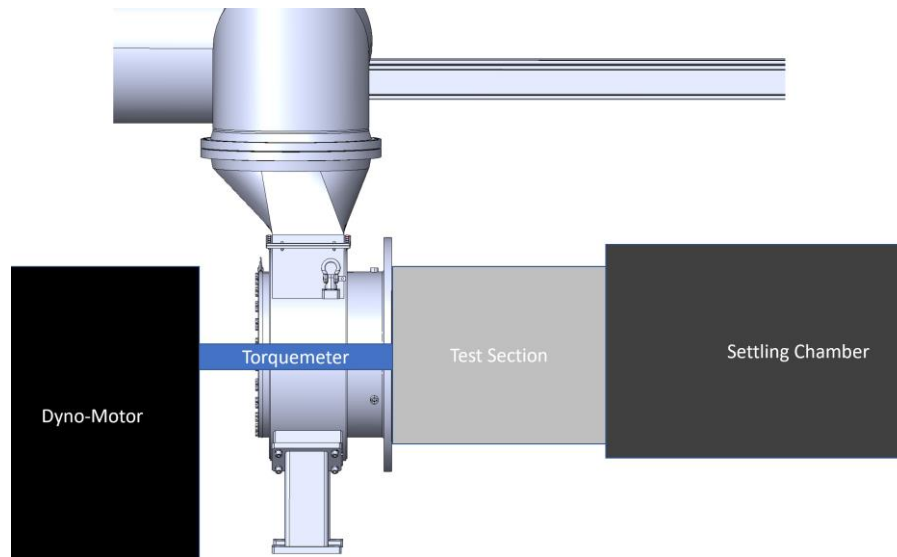


Figure 2-15. Diagram of PT-2 showing location of the torque meter.

A diagram of the required splitting and transmission is shown in Figure 2-16. The blue box labeled “T” represents the torque meter; the black bars spanning either side of the torque meter represent the moment arm used to apply torques to the sensor. The same pulley system representing the block and tackle shown in Figure 2-3 is shown on the left side of the diagram here. Instead of the moving block being coupled directly to a sensor, it is fixed to a pulley to allow the applied load to be split evenly between two lines. The two pulleys mounted directly to the right of the moving block are positioned to keep the two lines parallel with the load axis to avoid cosine losses. From these two pulleys, each line can be routed to a final set of pulleys which route the load to the moment arm, providing a counterclockwise torque to the torque meter. With this pulley system, all the pulleys and cables downstream of the moving block are transmitting the load, whereas the upstream pulleys are transmitting the effort, which requires them to have higher loading specifications than the upstream pulleys. There are various other pulley system architectures which could produce the same effect; two block and tackle sets could be used, for example, with the moving block of each coupled to the moment arm directly. This would require many more pulleys, which has no effect on the mechanical advantage in this particular case but would be significantly more expensive.

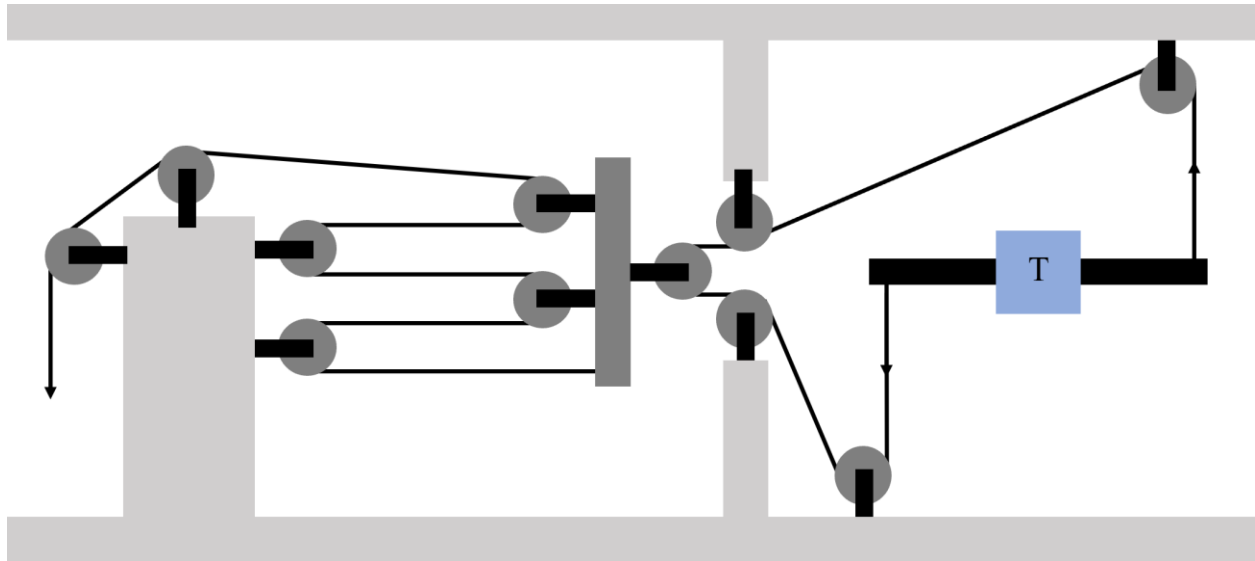


Figure 2-16. Diagram of the load-end pulley system.

Designing a rigging to host the pulley system shown in Figure 2-16 requires a similar discussion of tradeoffs for different methods of securing the rigging as was had for the thrust stand rigging. Here there are no net axial or tangential forces acting on the system, but there will be a moment that needs to be resisted. If a similar t-slotted frame was used to host this pulley system, it would be subject to flipping. The initial concept for this rigging was to take advantage of the thrust stand rigging and make only a few modifications to host this new pulley system. Figure 2-17 shows a CAD rendering based on this concept. Like the THOR rigging, there is still a 500-pound load, but it is internal. This necessitates a duplication of the load bearing members to host the downstream pullies. There are also rails placed to support the block and tackle and prevent dangling and load components due to their weight. This was removed after the validation tests were conducted because, after the first weight was added, the lines in the block and tackle were completely taut with an imperceptibly small angle. The moment arm is provided by a large disk, which is supported on an axel and connected to the rigging. This whole assembly would be placed with its main axis (defined the block and tackle and torque disk) in line with STARR's rotation axis such that the torque disk could be coupled to the torquemeter.

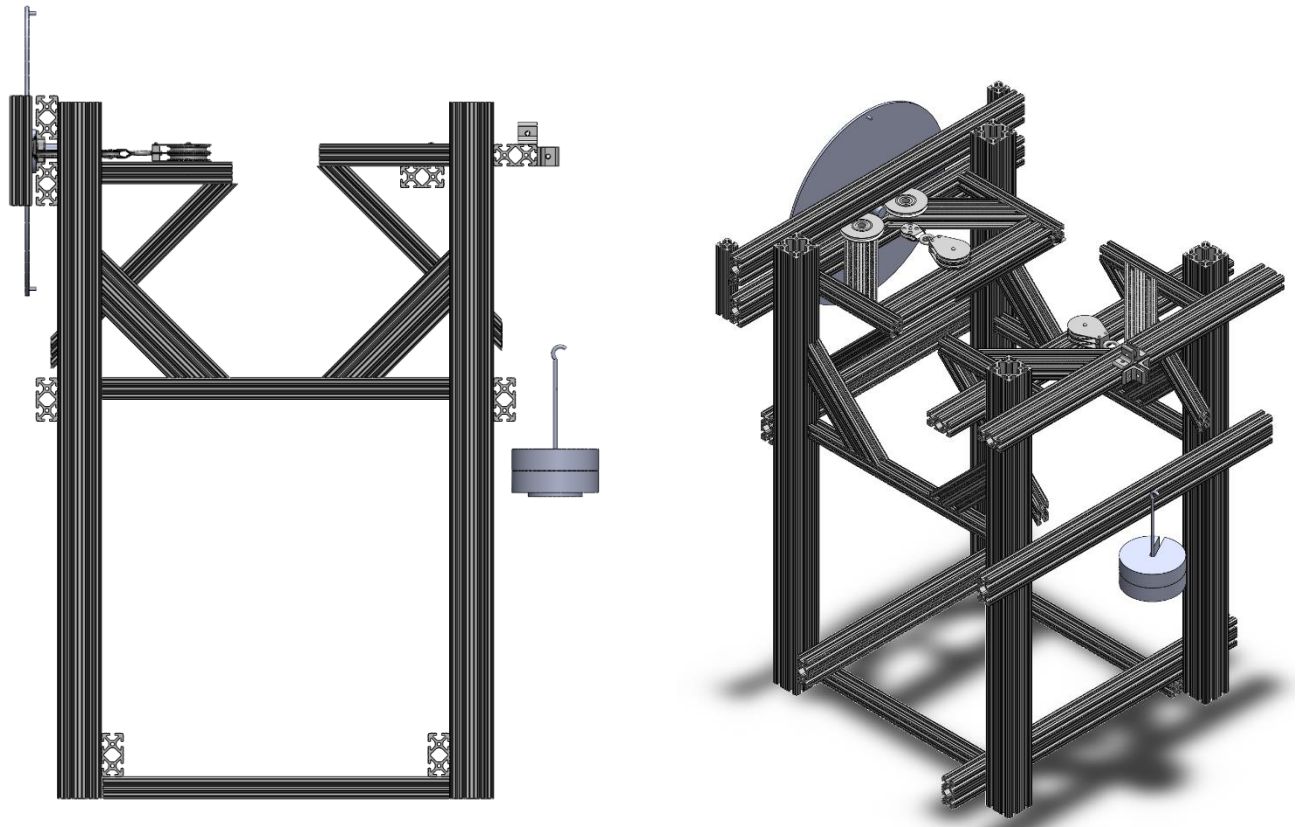


Figure 2-17: CAD rendering of a conceptual modification to the THOR calibration rigging for torque application.

The other option is to secure the rigging using the facility. A key difference between the torque application and the axial load application that makes this a more feasible option is the plane in which the tensions are carried. For the THOR calibration rigging, this plane was parallel with the floor and in line with the engine's main axis, and there was no existing facility hardware that could be used as hardpoints aligned with that plane. In this case, the plane is parallel with the test section anulus and coincident with the turbine coupling. This allows the test cell gantry crane to be used as a hardpoint. There is also a slotted concrete slab as a base to the STARR rig, which can be used to place non-permanent fixtures in the floor. The accessibility of these mounting points made a facility mounted rigging a more attractive option for the STARR calibration system. A CAD rendering of this type of rigging is shown in Figure 2-18.

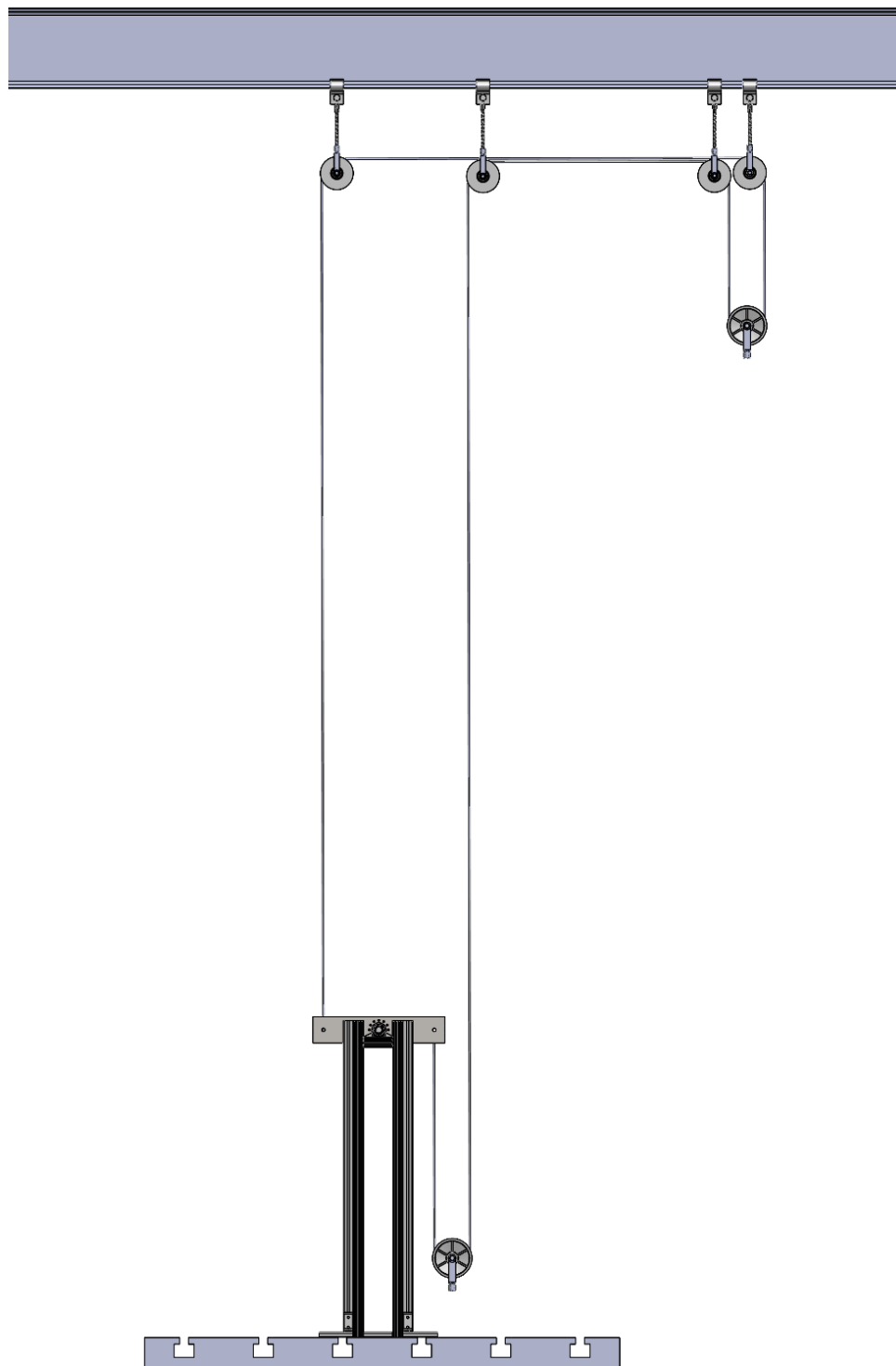


Figure 2-18: A CAD rendering of the torquemeter calibration rigging

The block and tackle are not included in the figure; the fixed block would be secured to the test cell floor with the moving block fixed to the pulley seen hanging from the gantry in the top right of the figure. This pulley splits the load, which is then carried along the gantry and routed down toward the torque bar. A final pulley is needed to rotate one of the lines 180 degrees so that it can pull downward. The torque bar is supported by an axle, which is mounted on a stand constructed from t-slotted framing, like the framed rigging discussed above. This feature was deemed unnecessary as the torque bar weight can be supported by the torquemeter arm, and the net forces acting on the torque bar, excluding weight, are only due to the difference in tension between the rising and falling lines, which will be very small. Figure 2-19 shows a detailed view of the cable routing, which allows the gantry mounted pulleys to occupy the same plane. The outside pulleys are mounted slightly higher than the inside pulleys, which allows the outside cable to pass above the inside pulleys through the fork of their clevis'. Not shown in this picture are three threaded rods tipped with eyelets which are placed between each pulley to provide a fixed separation and resist the inward forces acting on the pulleys.

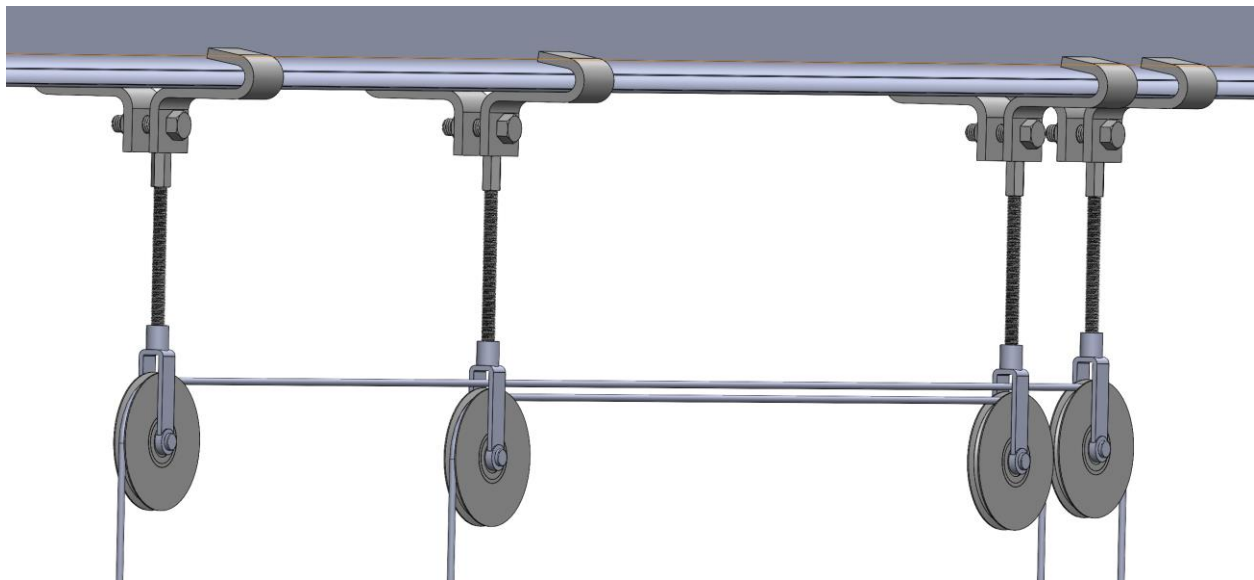


Figure 2-19: A detailed view of the cable organization within the gantry transit pulleys.

The conceptual framed rigging shown in Figure 2-17 featured a torque disk, whereas this facility mounted rigging has a torque bar. This change is inconsequential because the coupling between the cables and the torque disk were simple pegs or holes which the cable would loop

through, not allowing for the wrapping of the cable around the perimeter of the disk. Wrapping the cables around a torque disk is the best configuration for this system because it provides a constant moment arm through angular deflections of the disk; however, this would necessitate custom manufacturing or the purchase of an incredibly large pulley. Both options were prohibitively expensive. Using a torque bar will have a variable moment arm, but the errors this introduces can be mitigated by measuring the angle of the bar at each calibration step.

The rotary torquemeter measures torque on its rotating shaft. Calibrating the sensor with non-rotating static torque requires the shaft to be anchored. The torque bar will be coupled to the turbine side coupling of the torquemeter; the dyno-motor side of the torquemeter will be anchored. All other components of the rigging are being used per their specifications and are chosen such that they can support the 250-pound tension. The structural integrity of the torque bar and anchor is confirmed through FEA structural analysis. The parts are custom made from 1/8" stainless steel plates with bolt patterns matching the torquemeter coupling. For the simulation, the holes for cable mounting on the torque bar and for securing the anchor have walls set as fixed surfaces, and a torque of 350 foot-pounds is distributed evenly between the bolt pattern holes. The results of the analysis are shown in Figure 2-20.

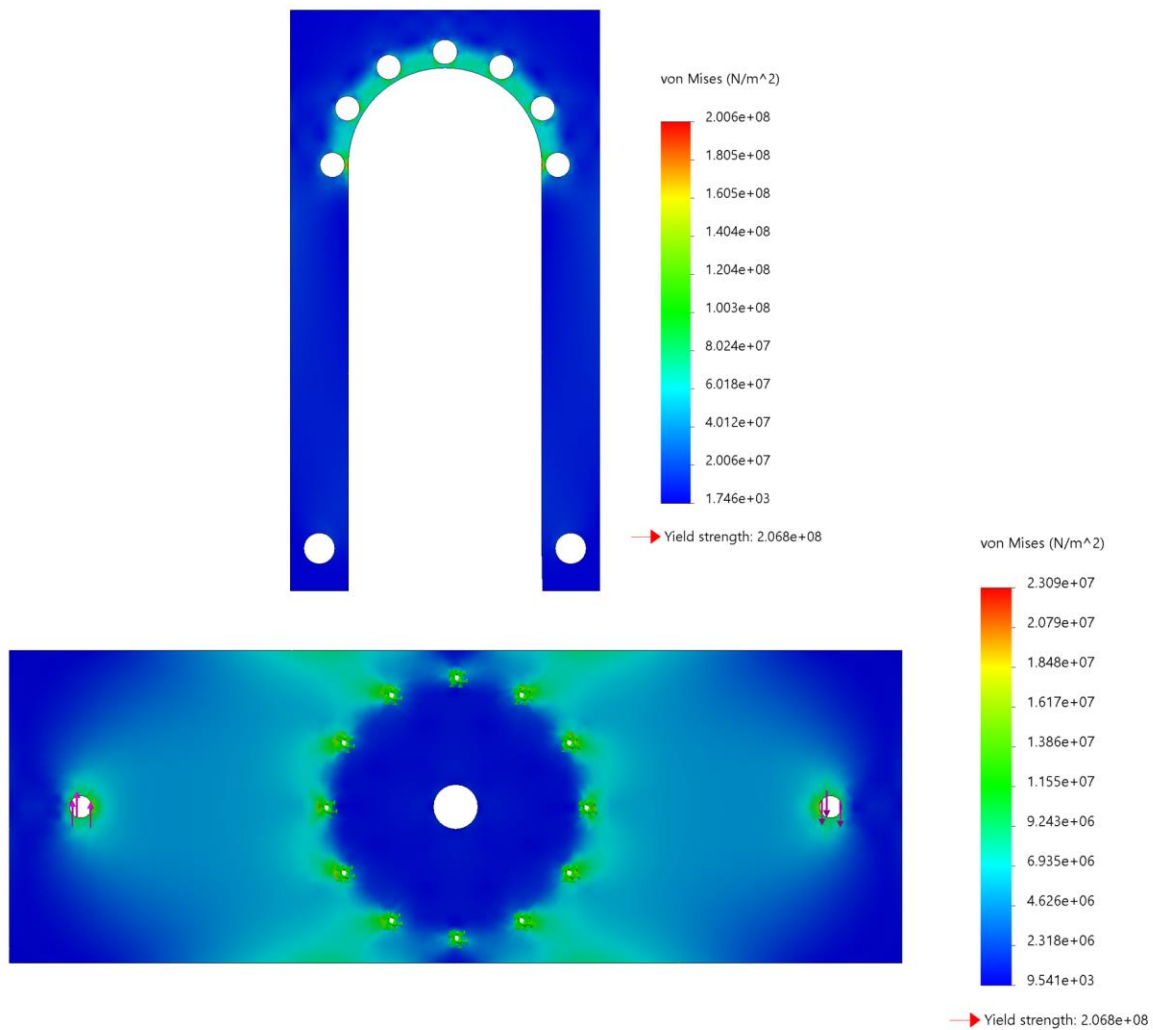


Figure 2-20: Figures showing the stress distribution for the torquemeter calibration anchor (top) and torque bar (bottom)

2.3 Calibration

2.3.1 THOR thrust stand

The calibration rigging for THOR described in the previous section was constructed and successfully mounted to the THOR thrust stand. Figure 2-21 shows the calibration system fully loaded while mounted to the thrust stand, with the interface shown in center frame: here the structure of the calibration stand abuts the fixed, lower frame of the thrust stand. The weights can be seen stacked on the high hanger in the lower right corner of the image. The effort is transmitted

to the same pulley system used for the validation test described in section 2.1.2. The block and tackle can be seen suspended by the load in the center frame of the image. The moving block is hooked to a 7x19 construction 3/16” steel cable which is aligned to apply the load along the central axis of the THOR engine.

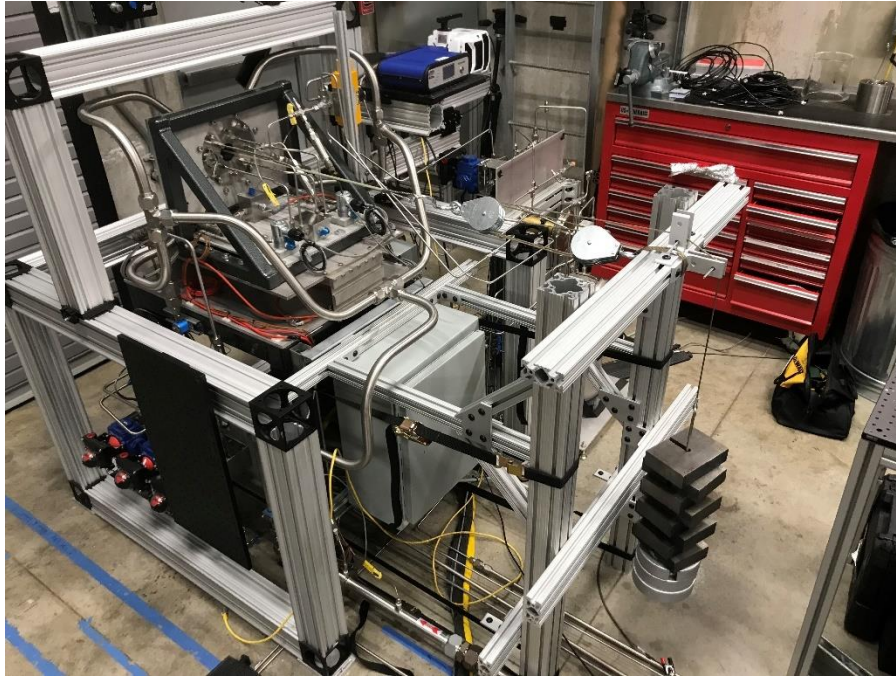


Figure 2-21: Calibration rigging mounted to THOR thrust stand.

The load is applied to the mounting fixture shown in Figure 2-22. This component is constructed from a 6x1.5x1.5” section of t-slotted framing. A vertical mill was used to drill holes matching the THOR inner body bolt pattern in the center of the extrusion and a channel on the outward face to secure the load carrying cable. The outer body of the combustion chamber and four sections of thin tubing were removed to accommodate the calibration rigging.

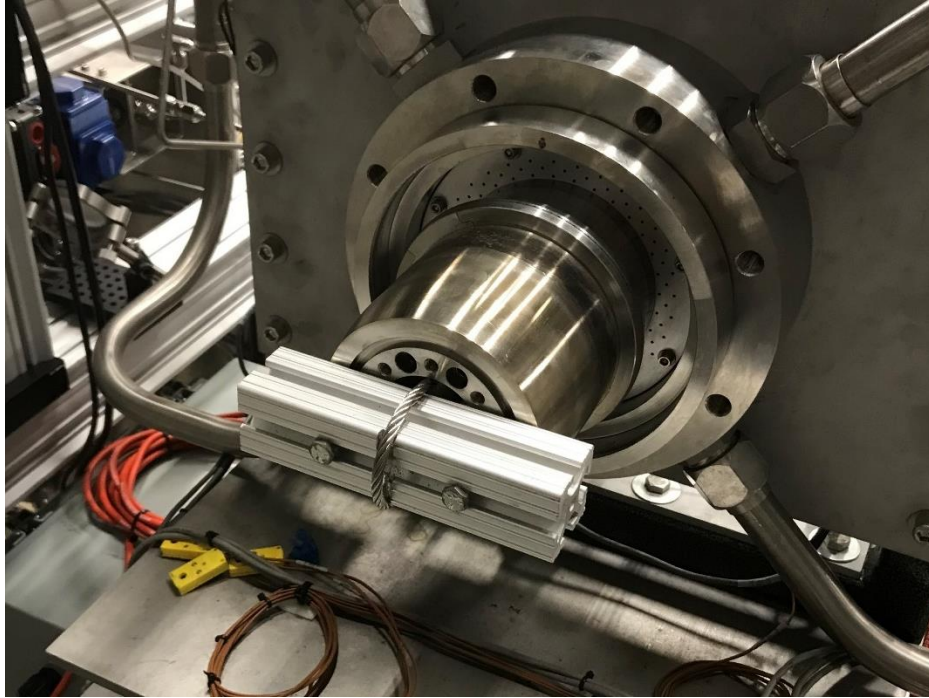


Figure 2-22: A picture of the load mounting fixture secured to the THOR inner body.

The output of the FUTEK LC450 2,000 lbf loadcell installed in the thrust stand was acquired at 2,000 Hz by a National Instruments X Series PXIe-6375 Multifunction I/O Module. A 5VDC excitation voltage was provided to the sensor by a FUTEK Model IAA100 Analog Amplifier. The calibration procedure is identical to that described for the validation test, with all the weights being loaded onto the high hanger one at a time and then unloaded. The raw data collected for the first trial is shown in the left plot of Figure 2-23.

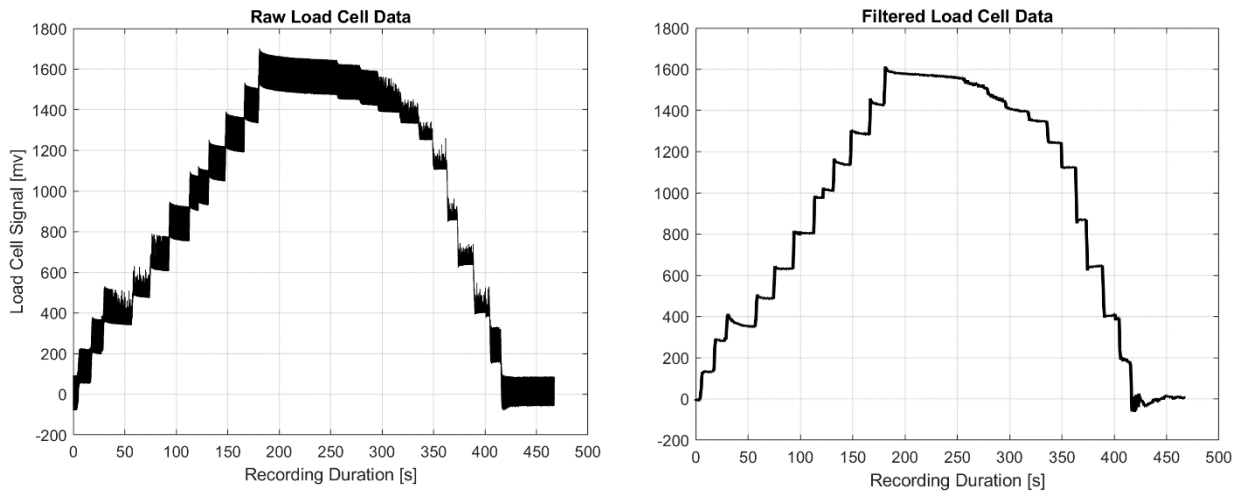


Figure 2-23: Raw and filtered data collected during the first calibration loading cycle.

There is significant noise caused by the voltage supply, which cites a noise level of 10 mVpp, and by electromagnetic interference present in the test cell. The data relevant to the static calibration of the thrust stand does not include any high frequency content, so a digital lowpass filter is used to remove all frequency components above 2 Hz. The filtered data is shown in the right plot of Figure 2-23. The filtered data clearly shows the trends of the load cell during the test, with the addition and removal of weights visible as discontinuous steps. The hysteresis described in the validation test is also present, with the steps produced by the removal of the first few weights being very small. There are also artifacts of non-ideal sensor performance: occasionally, the addition of weight results in a spike in sensor voltage which relaxes over a period of roughly 20 seconds; there is also a significant low-frequency oscillation of the signal at the end of the test. The first of these is an expected behavior of the sensor and can be mitigated by waiting enough time for the sensor to relax before adding the next weight. The second is a more serious obstacle to calibration. When these oscillations were observed, there was no significant physical disturbance to the calibration system occurring; the cause is likely a variation in excitation voltage to the sensor or some other significant source of current induction into the signal wires. During the first test, there was active experimentation taking place at Zucrow Labs, so a possible cause is the use of high-power radios common during test setup and operations. The fourth and fifth data sets were collected late in the evening with no other testing occurring, and there were no oscillations observed in these data.

The sensor data was converted into a series of signal/load pairs by averaging the sensor output over 0.5 second intervals in stable regions of each step. It is critical to the calibration that the averaged signal value is caused by the expected load condition. The data shown in Figure 2-23 features an anomalous step during the loading at around 1000 mV. This was caused by some slipping of the pullies unrelated to the application or removal of weights. Figure 2-24 shows the placement of one of weights during the calibration. It is critical to assure that the placement and removal of weights from the high hanger is done with extreme care. Any added force, swinging of the weights, or bumping of the calibration rigging can cause slips and a new load point. The signal/load pair for this step was evaluated at the first step; the anomalous second step was ignored.

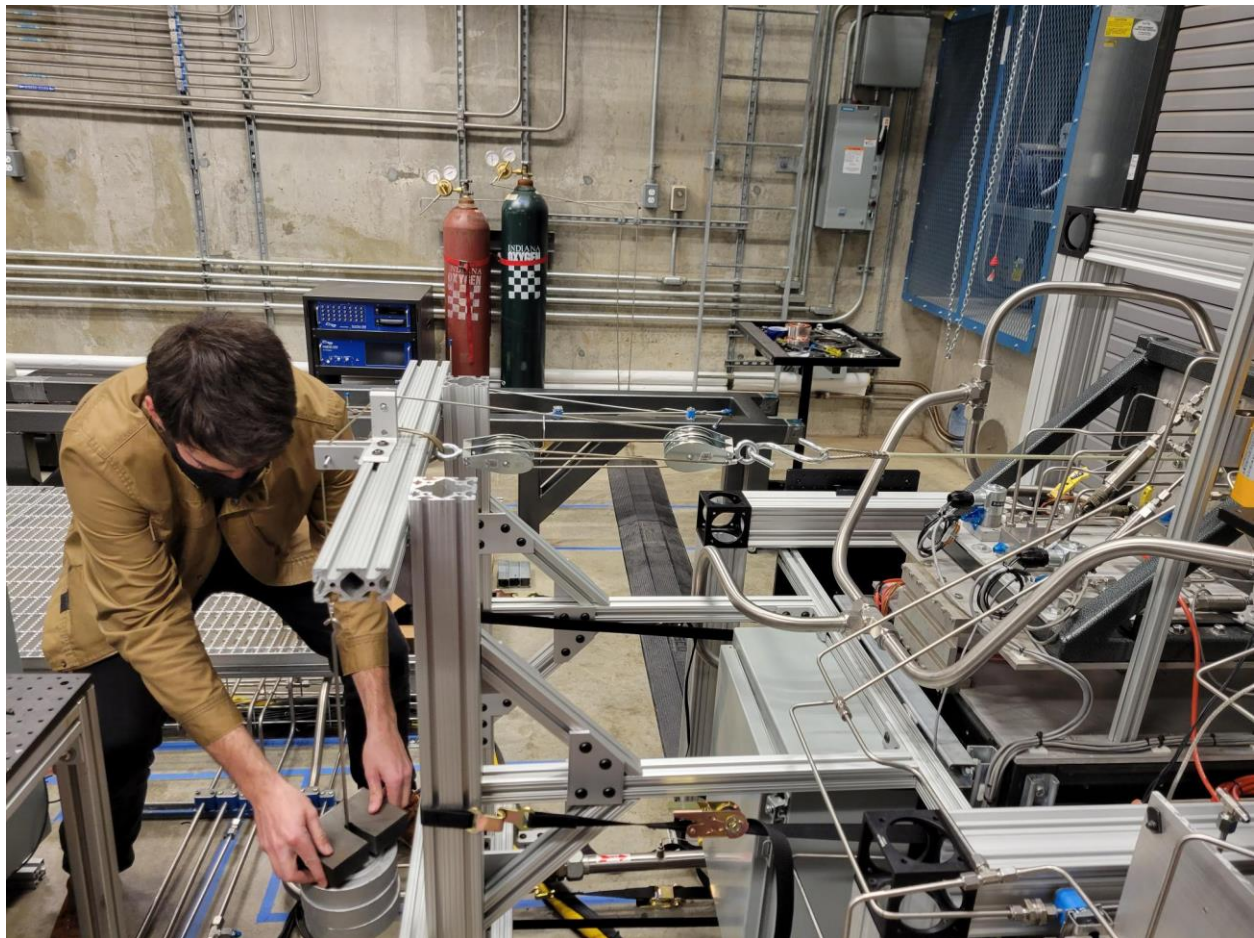


Figure 2-24: A picture of weights being added onto the THOR calibration rig.

The signal values collected from the sensor data are plotted with respect to effort in Figure 2-25. The same hysteretic behavior observed in the model and the validation test is observed.

However, there is a much larger spread of signal values for a given loading condition than seen with the hanging scale used for the validation test. This spread is due to sensor drift, which was observed both during the noisy daytime test environment and in the nighttime test environment.

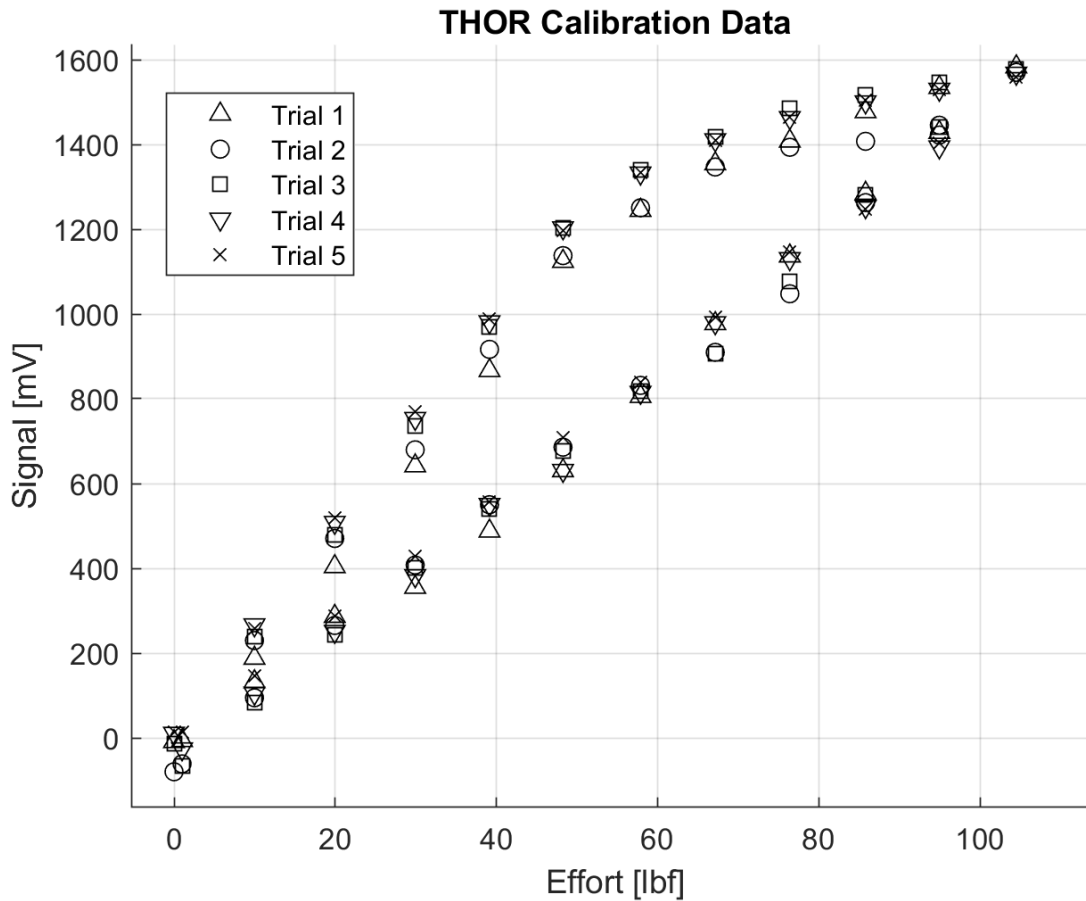


Figure 2-25: Measured signal plotted vs effort for the THOR calibration.

The sensor drift heavily impacts the achievable accuracy of the thrust table. The uncertainty of the calibration constants and subsequent thrust measurements has a 100% sensitivity to the absolute uncertainties of both the effort and the signal. The sensor and amplifier specifications provide an absolute uncertainty of 1 mV, however the observed variation in signal for the same load condition gives an absolute uncertainty of 75 mV. For the purposes of the subsequent error calculations, only the specified uncertainty of the sensor and amplifier will be considered. The variation of these values from a linear fit due to the sensor drift will be accounted for in the uncertainties of the calibration constants.

The calibration process used for the validation test and shown in Figure 2-8 is applied here to generate the calibration constants for the THOR thrust stand. For the convenience of thrust data processing, the constants are generated for thrust as a function of Voltage. A plot of applied loads vs. sensor output is shown in Figure 2-26. The values of the slope and offset for this line and their associated uncertainties are listed in Table 4.

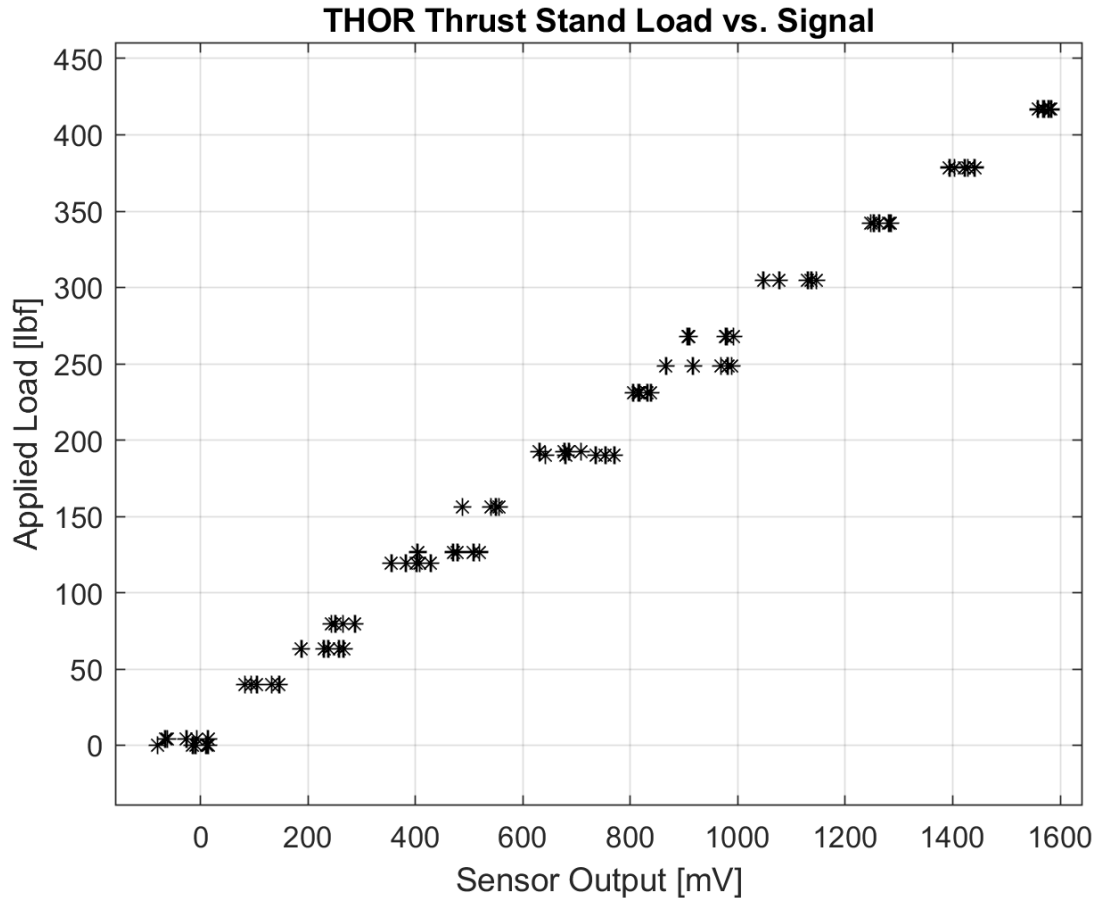


Figure 2-26: Calibration plot for THOR thrust stand.

The thrust stand response is linear with an R-square of 0.9938, which is expected from thrust measuring systems, but not a given. The slope is also very tightly defined with a percent error of 0.19%, however, the sensor drift mentioned above results in a very large uncertainty on the offset with a percent error of 100%. Data from the load cell calibration certificate is listed in the table below and shows that forces applied to the thrust stand are not wholly transmitted to the sensor; 25% of the thrust is dissipated elsewhere in the stand, likely in the stiffness of the flexures,

one of which can be seen supporting the thrust table in the center right of Figure 2-24, which are constructed with 0.1” thick sections of stainless steel. The flexural modulus of these parts is much higher than ideal, allowing them to partially support axial loads applied to the thrust stand. The expected voltage in an unloaded state is given by the sensor specifications as -10 mV, this gives an expected offset of 0.2lbf for the load cell and 0.26lbf for the thrust stand, which is within the calculated error bounds.

Table 4: Calibration results for THOR thrust stand.

	m [lbf/V]	b [lbf]	R²
Thrust Stand	261.0±0.5	10 ±10	0.9938
Load Cell	200	0.164	1.000

The results of the calibration can be used to process load cell data from THOR experiments into thrust data. The large offset uncertainty will result in thrust uncertainties on the order of 10 lb. Experimental thrust values collected for a range of oxidizer mass flows during THOR hot fires are plotted in Figure 2-27.

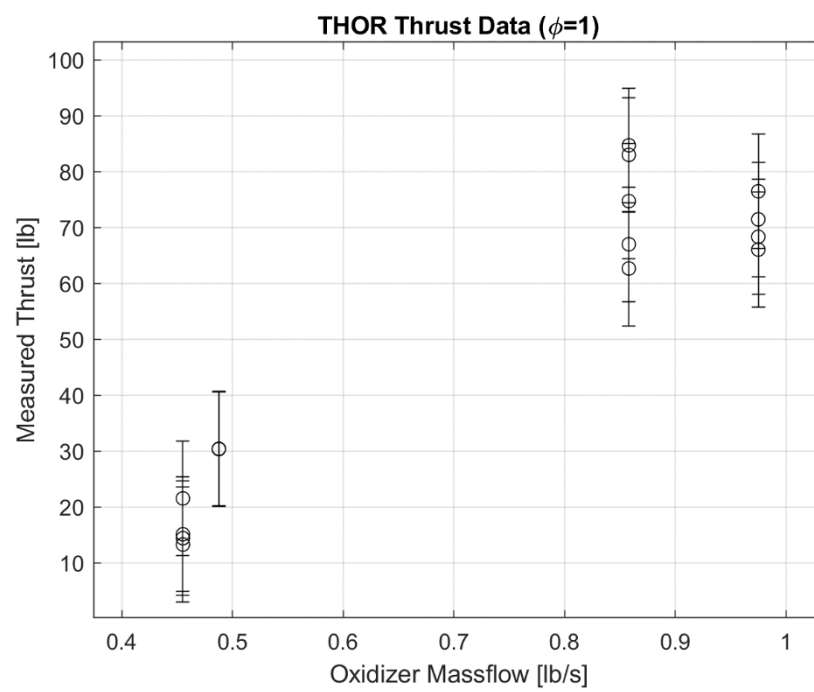


Figure 2-27: Experimental THOR thrust data plotted with respect to oxidizer mass flow rate.

3. LASER OPTICS NACELLE

Steady state operation of optical components in high temperature flow requires cooling to maintain internal temperatures within operational ranges. Two cooling jacket designs were considered, a pipe coil jacket configuration, and a conventional jacket configuration. Cross-sectional schematics of these designs are shown in Figure 3-1. Several prospective coolants were also investigated, including water, diluted glycol, and gaseous nitrogen.

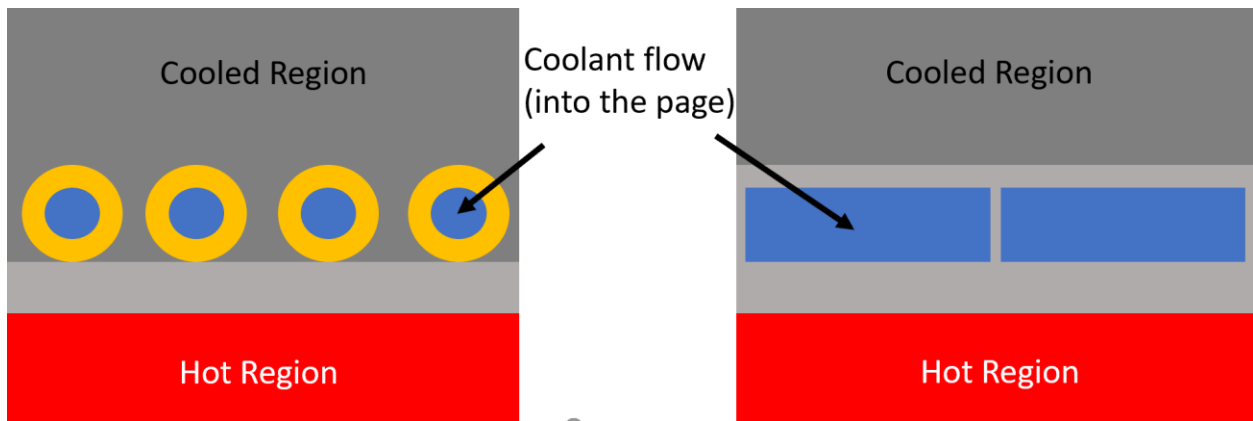


Figure 3-1. Cross-sectional views of a pipe coil cooling jacket (left) and a conventional cooling jacket (right).

3.1 Model

This section details the model used to estimate the convective heat fluxes acting on the probe, analyze the effectiveness of different cooling schemes, and optimize parameters within those schemes. The procedure is largely influenced by the cooling jacket analysis presented by Heister, Anderson, Pourpoint, and Cassady [34].

3.1.1 Estimation of Flow Conditions

Convective heat flux through a surface is dependent on fluid properties near that surface. These properties can be estimated for a highly compressible and high enthalpy flow assuming isentropic flow relations and making use of normal and oblique shock relations and Prandtl-Meyer expansion [35]. A basic diagram showing the different probe faces where flow properties need to

be evaluated and which flow processes determine them is shown in Figure 3-2. For an idealized geometry with infinitesimal edge radii, flow over the top of the probe (face 1) and over the side faces (face 4, not shown) will have the same properties as the freestream flow (face 0). An oblique shock will form when the flow is turned by the leading wedge; conditions downstream of this shock are assumed for face 2. The flow is allowed to expand at the downstream edge of face 2; conditions at the lower face (face 5) are determined assuming Prandtl-Meyer expansion. These flow properties are also assumed as the upstream conditions for the calculation of properties near face 3. Similar propagation of the oblique shock and expansion fans is used to compute the properties at the faces of the support stem, 6 and 7, which has a diamond cross-section.

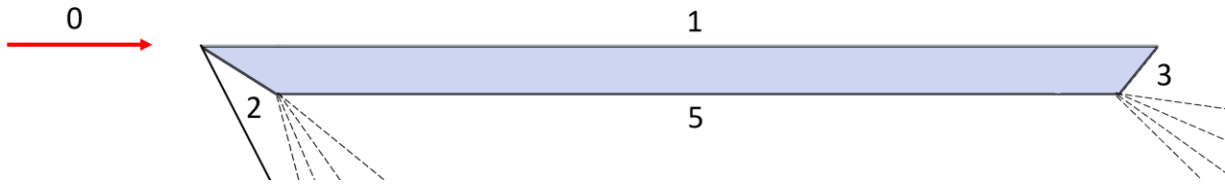


Figure 3-2: A diagram of relevant faces and flow phenomenon for the estimation of probe heat flux.

The free stream flow is dry air and has a 16-bar total pressure, a 0.01-bar static pressure, and a 200K static temperature, giving a Mach number of 6.01. The results of the calculations described above are listed in Table 5. Face 3, which represents flow near the aft face of the probe, produces unrealistic flow properties due to the large turning and the high Mach number upstream of this section due to the expansion over face 7.

Table 5: Flow properties near probe faces using isentropic flow relations.

	0	1	2	3	4	5	6	7
Mach	6.01	6.01	2.34	27.1	6.01	3.96	2.51	3.59
P_s [pa]	1000	1000	17,800	0.0884	1000	125	659	7.63
T_s [K]	200	200	787	27.2	200	191	348	97.2
ρ [g/m³]	17.4	17.4	78.9	0.0113	17.4	2.30	6.60	0.274

These results were used for the preliminary cooling analysis of the probe. A 2D Reynolds-averaged Navier-Stokes CFD analysis was also performed on the same geometry shown in Figure 3-2 with the support (faces 6 and 7) removed to provide better estimates of flow properties and cooling performance. The computational domain is sized to represent the wind tunnel test section. The inlet has a far-field boundary condition with static conditions and Mach number specified. The outlet has a pressure outlet boundary condition with static conditions defined. The boundary condition specified on the top and bottom walls is no-slip, and the probe body walls are isothermal. The purpose of this CFD analysis is only to validate the flow properties near the wall. The cooling analysis takes free stream velocity as an input, so properties very near the wall and cells within a y^+ of 1 are not critical to the utility of this analysis.

Ansys Fluent is used as the RANS solver with a K-Omega SST turbulence model. The unstructured mesh produces unclear shock boundaries, but the fluid properties should provide a good validation for the analytical equations used in the preliminary analysis and better estimations for the flow properties in the separation region off the trailing edge. Table 6 shows values probed from the CFD results at regions outside of the boundary layer but near to the walls. These are listed parenthetically while the values from Table 5 are listed normally.

Table 6: Comparison of isentropic flow relations to CFD values (CFD listed parenthetically).

	0	1	2	3	5
Mach	6.01 (5.98)	6.01 (5.86)	2.34 (2.30)	27.1 (0.181)	3.96 (3.86)
P_s [pa]	1000 (1050)	1000 (1260)	17,800 (17,600)	0.0884 (210)	125 (1,880)
T_s [K]	200 (206)	200 (206)	787 (792)	27.2 (594)	191 (413)
ρ [g/m³]	17.4 (17.2)	17.4 (18.4)	78.9 (75.7)	0.0113 (0.00618)	2.30 (13.8)

Values for faces 4, 6, and 7 are absent from the above table because they are not represented in the 2D geometry. In the remaining faces, there is impressive agreement between the analytical and numerically generated values, with the largest discrepancy (excluding face 3) being in the region below the probe (face 5). The analytical values for face 5 were propagated from the free stream through an oblique shock and then through an expansion fan; the sequential application of analytical models compounds inaccuracies, which explains the wider variance for this face. The properties for face 3 are wildly different (and more realistic) than those calculated analytically;

this is because the CFD accurately captures flow separation, which is not predicted by Prandtl-Meyer expansion. The values predicted by the CFD are used for 1-D heat transfer model described in the following section.

3.1.2 1-D Heat Transfer Model

The steady state temperature distribution along a coolant line can be estimated by calculating the heat flux into an initial fluid element and solving for the subsequent temperature rise then repeating the calculation in the next fluid element the incremented temperature. Figure 2-1 shows a diagram of the fluid element with length Δx . The temperature profile illustrated to the right of the element shows how the hot flow temperature increases to a recovery temperature as it slows in the boundary layer. The heat transfer between the hot and cold flows creates discontinuous temperature differences between the recover temperature and the outer wall temperature. A similar temperature difference is present between the inside wall temperature and the coolant temperature.

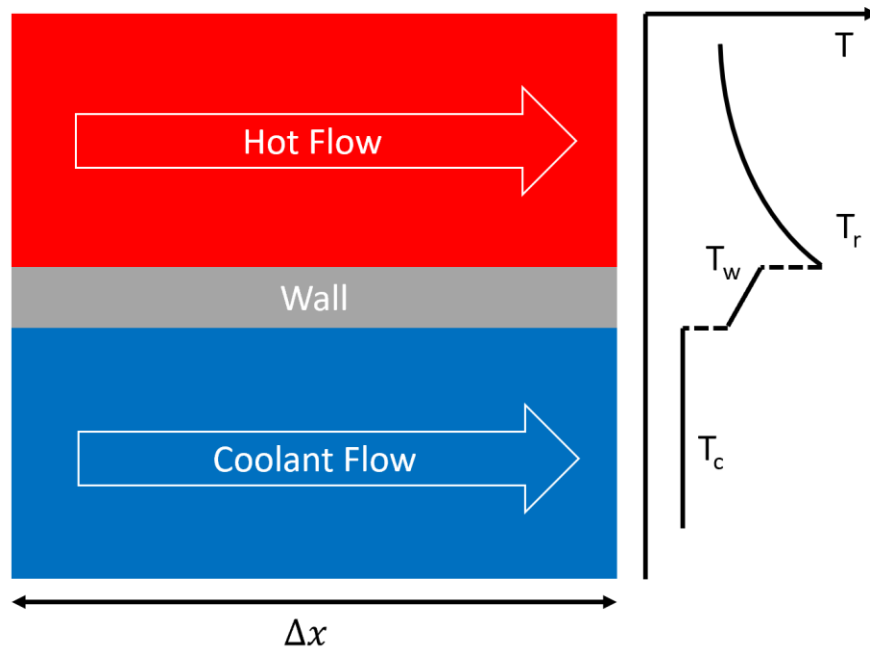


Figure 3-3: A diagram of the 1-D fluid element and its associated temperature profile.

Convective heat transfers are assumed to be much larger than radiative heat transfers. If the latter are neglected, the heat flux into the wall can be written as

$$\dot{q} = h_g(T_r - T_w) \quad (18)$$

where \dot{q} is the heat flux in Watts per square meter, h_g is the convective heat transfer coefficient for the hot flow, and T_r and T_w are the hot flow recovery temperature and outside wall temperature respectively. Similarly, the heat flux into the coolant element can be written as

$$\dot{q} = h_l(T_{wl} - T_l) \quad (19)$$

where h_l is the convective heat transfer coefficient for the coolant, and T_{wl} and T_l are the coolant side wall temperature and coolant element temperature.

The outside wall temperature cannot be solved for analytically; an iterative procedure is used to compute this value by evaluating the two equations above at a guessed wall temperature and repeating the calculation with different wall temperature values until the heat flux into and out of the wall are suitably close. The heat flux into the wall is computed by first calculating the recovery temperature with

$$T_r = T_s \left(1 + \frac{\gamma - 1}{2} r M^2 \right) \quad (20)$$

where r is the recovery factor which, for a turbulent free boundary layer, is defined

$$r = Pr^{1/3} \quad (21)$$

The hot flow convective heat transfer coefficient is computed from the following Nusselt number correlation for turbulent flow over a flat plate [36]

$$Nu = 0.037 Re_L^{0.8} Pr^{\frac{1}{3}} \quad \begin{matrix} 0.6 \leq Pr \leq 60 \\ 5 \times 10^5 \leq Re_L \leq 10^7 \end{matrix} \quad (22)$$

The probe surfaces are essentially flat plates, and the hot flow Prandtl number is 0.85. The Reynold's numbers at the probe faces varies from 1.5×10^6 to 2×10^6 , so this correlation is well suited to estimate the convective heat transfer coefficient. With the previous equations, the heat flux into the wall is computed, and now the inside wall temperature can be computed assuming conductive heat transfer:

$$T_{wl} = T_w - \frac{\dot{q}t_w}{k} \quad (23)$$

Here t_w is the wall thickness and k is the wall thermal conductivity. This equation can easily be expanded to account for added material layers for different heat exchanger configurations. The Dittus and Boelter equation as introduced by McAdams [37] is used to estimate the coolant convective heat transfer coefficient:

$$Nu = 0.026Re^{0.8}Pr^{0.4} \quad (24)$$

This form of the Dittus and Boelter equation is described as applicable to turbulent pipe flows [34], however it does differ from other cited forms of the equation. The coefficient of 0.026 is typically used when the fluid is being cooled while the exponent of 0.4 is used for fluid being heated [38]. A similar correlation for turbulent pipe flows with Reynold's numbers between 40,000 and 400,000 was found with a coefficient of 0.027 and an exponent of 1/3 [36]. The Reynold's number of the coolant is consistent at around 1.2×10^5 , which is within the range. The similarity in the coefficients and exponent and the agreeable Reynold's range give suitable confidence in the correlation provided by equation (24). The hydraulic diameter of the cooling channels is used to compute the convective heat transfer coefficient, and, finally, the heat flux into the coolant can be computed and compared with the heat flux into the wall.

Once the value for wall temperature is converged, the change in temperature of the fluid element can be computed. This change is applied directly to the next fluid element with

$$T_{l(i+1)} = T_{li} + \frac{\dot{q}\Delta A}{\dot{m}c_{pl}} \quad (25)$$

where \dot{m} is the mass flow in the coolant channel and ΔA is the area of the fluid element contacting the wall. The coolant properties are updated based on the new temperature and the process is repeated. This procedure is summarized in Figure 3-4.

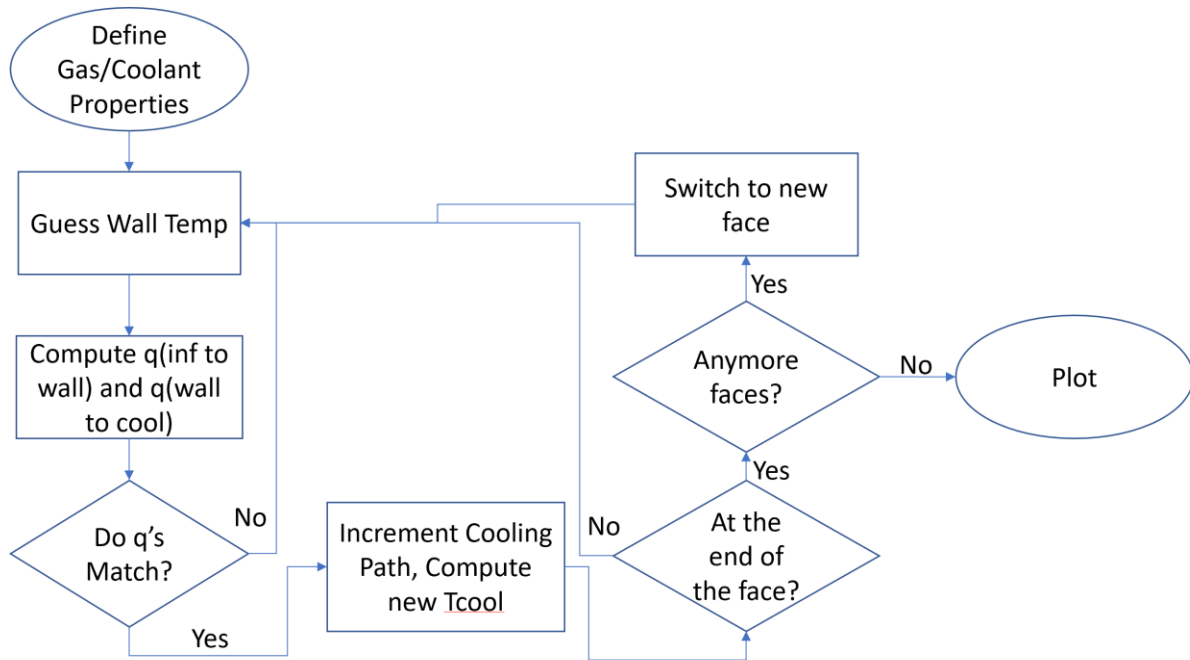


Figure 3-4: Flow chart for the cooling analysis

3.1.3 Parametric Analysis

The cooling analysis described above was used to inform several design choices for the probe. Figure 3-5 shows temperature profiles for two very different cooling architectures. The left plot represents a water based cooling architecture with copper tubing which layers the inside probe walls in a series of rows. The right is a gaseous nitrogen based architecture making use of much larger, straighter cooling channels. Figure 3-1 shows diagrams of these. The physical difference between the architectures is well illustrated by the horizontal axes of the plots which show the total length traveled by a fluid element in the coolant path. The reciprocating, tightly packed, tubes of the water based architecture result in extreme lengths of tubing and long residence times when compared to gaseous coolant traveling in straight channels. The discontinuities in the outside wall temperature result from the coolant path reaching a new probe face and different recover temperature and heat flux values. The calculation was configured to run the coolant through the faces with the highest heat flux first.

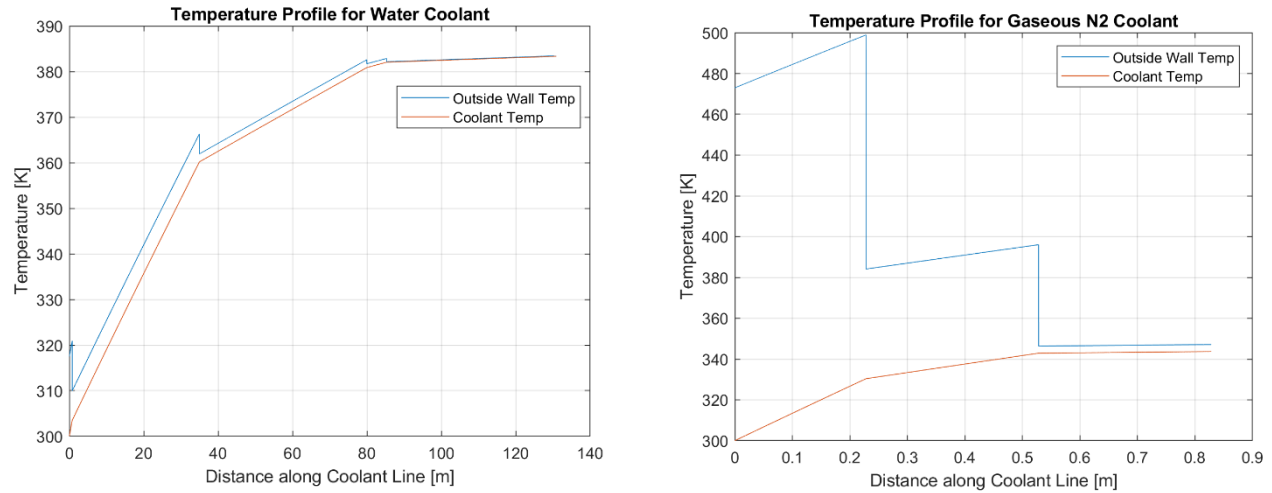


Figure 3-5: Plots of temperature profiles for water coolant (left) and gaseous nitrogen coolant (right)

Both architectures provide sufficient cooling, though the water-based system keeps the exterior wall temperature significantly cooler at the cost of higher complexity and an inability to be made open cycle. The nitrogen system is attractive despite the higher wall temperatures because of its reduced complexity, the high accessibility of pressurized nitrogen supply facilities, and the ability to vent the coolant into the wind tunnel instead of recirculating it. These plots also highlight the dependence of cooling effectiveness on channel geometry, which affects both the coolant flow speed and the surface area available for heat transfer. The nitrogen architecture is chosen for further analysis wherein this geometry is, along with other relevant parameters, optimized.

The head pressure supplied to the coolant has a large effect on the cooling performance. Figure 3-6 shows the wall temperature profile for nitrogen coolant with a head pressure of 10 bar and a head pressure of 1 bar. This was also generated with a different configuration of the coolant path, with the coolant passing by the face with highest heat flux closer to the middle of the path rather than the beginning. The lower head pressure results in a maximum wall temperature nearly double that provided by the higher head pressure.

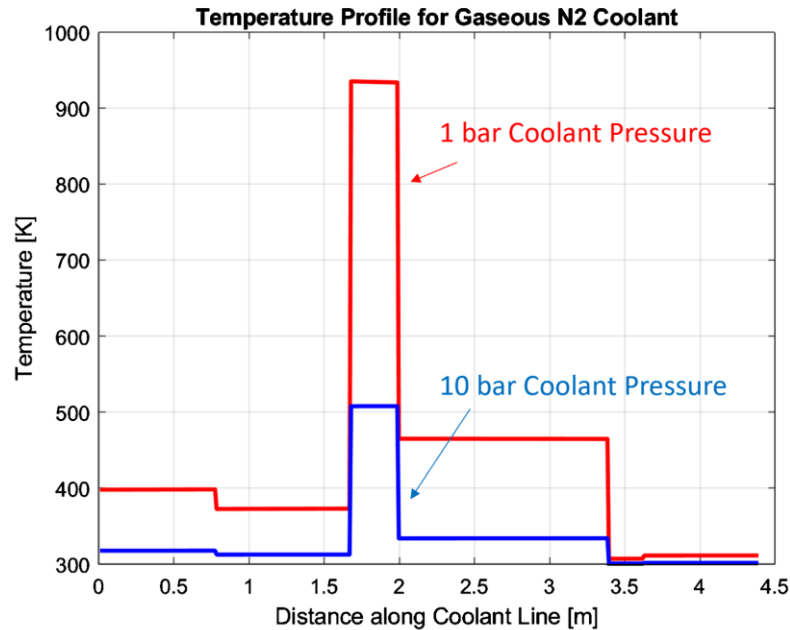


Figure 3-6: A plot of temperature profiles for a nitrogen cooling scheme at different heads

Higher head pressures clearly provide better cooling performance but also result in increased design complexity and weight to maintain structural integrity. For this reason, it is desirable to find a design point which provides sufficient cooling while minimizing the coolant pressure. This was accomplished by performing a parametric analysis on the maximum temperatures enabled by the cooling system. The left plot in Figure 3-7 shows how the max exterior wall temperature varies with different head pressures and coolant sonic areas. The relevant limitation on maximum wall temperature is the material limitation; to illustrate the required performance, surfaces representing the maximum operating temperature of aluminum, stainless steel, and Inconel are overlaid.

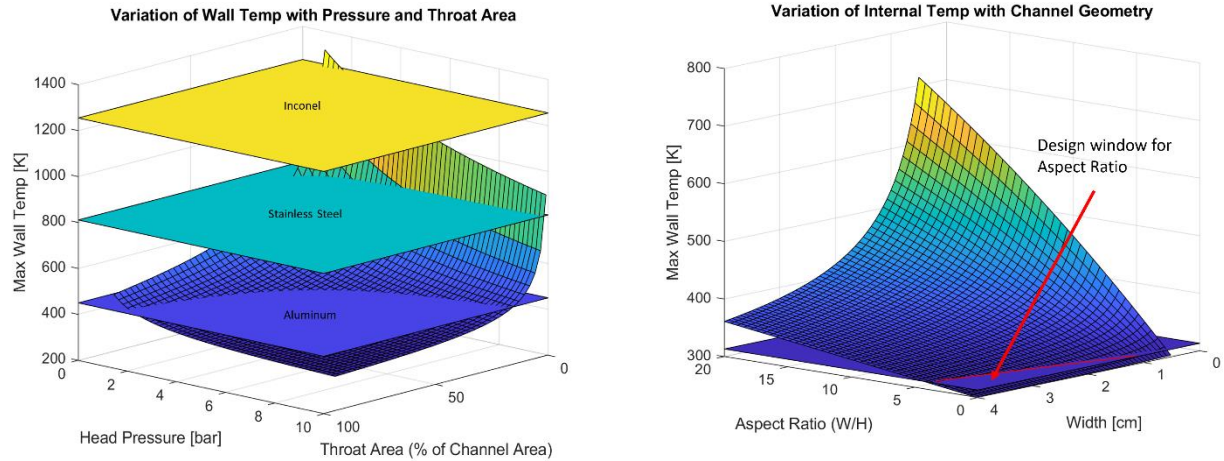


Figure 3-7: A plot of maximum wall temperature as it varies with sonic area and head pressure (left). And a plot of the variation in maximum internal temperature with cooling channel geometry (right).

The plot shows the expected trend with respect to pressure, with the lowest temperatures occurring at the highest head pressures. There is, however, a diminishing return for continued increases in pressure, with values higher than 5 bar providing very little additional cooling effectiveness. A similar trend is observed with the sonic area. The only material which inhibits the acceptable pressure and sonic area ranges is aluminum. Stainless steel can operate at all but the lowest coolant pressures and most restrictive sonic areas, and Inconel can nearly operate without any cooling at all. Weighing these performances with the need for reasonable material strength, stainless steel is the clear choice.

A more restrictive cooling requirement is the survival of optical components within the probe. The right-side plot in Figure 3-7 shows a similar plot but with the maximum internal temperature (which is assumed equal to the maximum coolant temperature) varying with cooling channel aspect ratio (defined as width of the area available for heat flux divided by the channel height) and channel width. A plane representing the maximum operational temperature typical to optical components of 40 degrees Celsius is overlaid.

The dependence of this temperature on channel geometry shows that larger widths (and larger heat flux areas) are beneficial to cooling effectiveness. Lower aspect ratios are also preferred. The limitation of optical component operational temperature is much more restrictive than the same for probe material with only a narrow corner of the design space providing sufficiently low

internal temperatures. The intersection of the temperature surface with the limiting plane forms a line with a slope nearly equal to one for aspect ratio as a function of width. This gives an interesting limiting relationship that can be used to determine the optimum channel geometry: the aspect ratio should be less than or equal to the channel width as measured in centimeters.

$$AR \leq W[cm] \quad (26)$$

3.2 Mechanical Design

This section catalogues the detailed design of the optical probe. While this probe is designed to accommodate a unique optical configuration, the same principles can be applied in a piecewise fashion to allow the cooling of individual optical components and the installation of complex and versatile optical paths in high enthalpy test environments.

3.2.1 Internal Optical Layout

A diagram of the optical components needed for FLASH MTV is shown in Figure 3-8. The probe body is shown in gray, and the write and read lasers are shown in red and blue respectively. The two beams enter the probe columnated from the bottom of the diagram and are redirected towards the main optical assembly. The write laser is focused, the read laser is formed into a sheet, and these are then combined and directed out of the probe body. The optical setup shown in the figure above can be built using THORLABS optical cage system and secured along dovetail optical rails mounted to the probe.

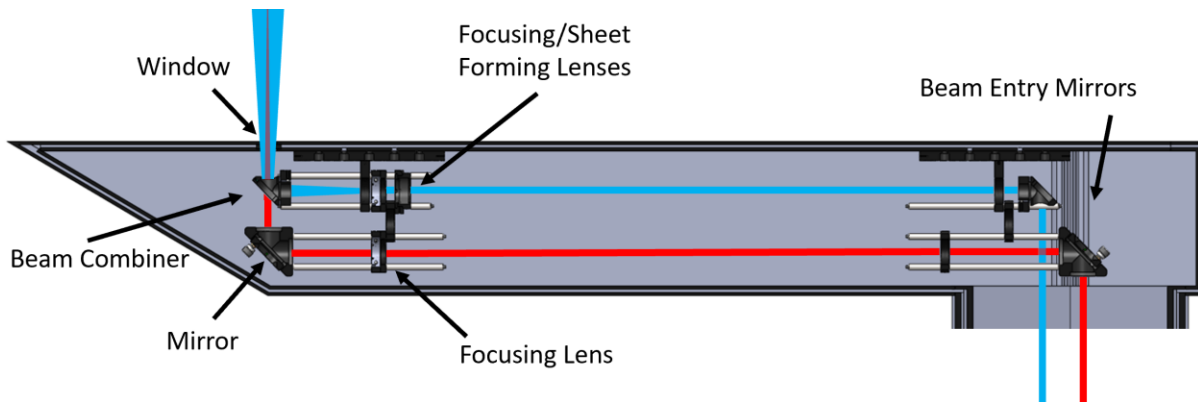


Figure 3-8: A CAD rendering of a FLASH optical setup using THORLABS components

The wavelength of the tagging laser can range from 800-1,064 nm while the wavelength of the PLIF reading laser is 284 nm. The respective lenses and mirrors must be suitable for transmission at these wavelengths. The window must provide high transmissibility for both lasers. A common material used for FLEET windows is UV fused silica which has a transmission range of 195 to 2,100 nm. This range is suitable for the read laser as well, so this is the material that will be used for the window.

3.2.2 External Nacelle (Probe Body)

The dimensions of the probe are largely determined by the size of the optical components and the needed configuration of optics in the test. Figure 3-9 shows a rendering of the full-scale probe. The facility this probe is intended for is a hypersonic free jet wind tunnel. The 50" extension of the probe allows the base to be mounted in the larger test cell while the probe tip and optical exit are placed within the jet nozzle. This configuration also accounts for the 36" height. The 3" width and 5.9" height of the probe head are the minimum dimensions to allow for the optical rails described in the previous section.

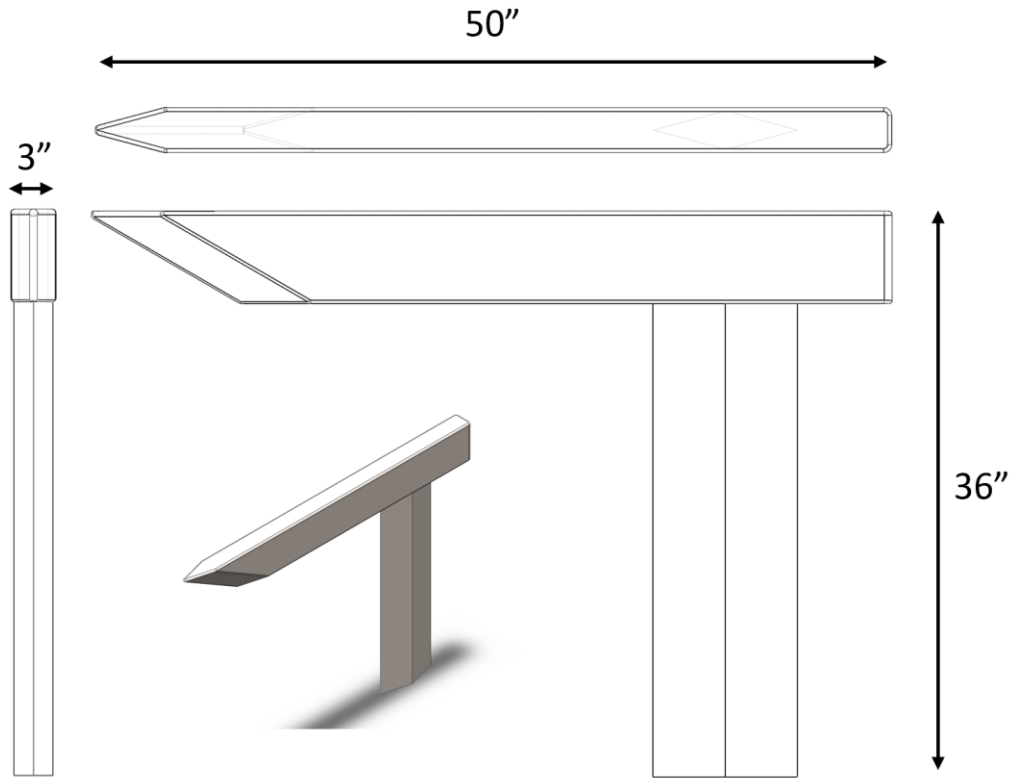


Figure 3-9: A CAD rendering of the full-scale optical probe with profile dimensions listed.

The leading-edge geometry was selected to provide the shallowest wedge angles while still allowing room for the optics to be mounted sufficiently far forward. A 30-degree angle between the vertical leading edge and the top surface was chosen. This same angle is used for the horizontal wedge. This configuration is intended to provide minimal disturbance to the flow over the top surface of the probe where the measurement region is, deflecting the oblique shocks expected to the underside of the probe.

A 3D RANS CFD analysis was performed on the geometry shown in Figure 3-9 to estimate the amount of flow disturbance above the flow. Vertical and horizontal slices of a Mach contour produced by this analysis are shown in Figure 3-10. The fluid domain for this analysis was much larger than indicated in the figures, with about one probe length upstream and two downstream.

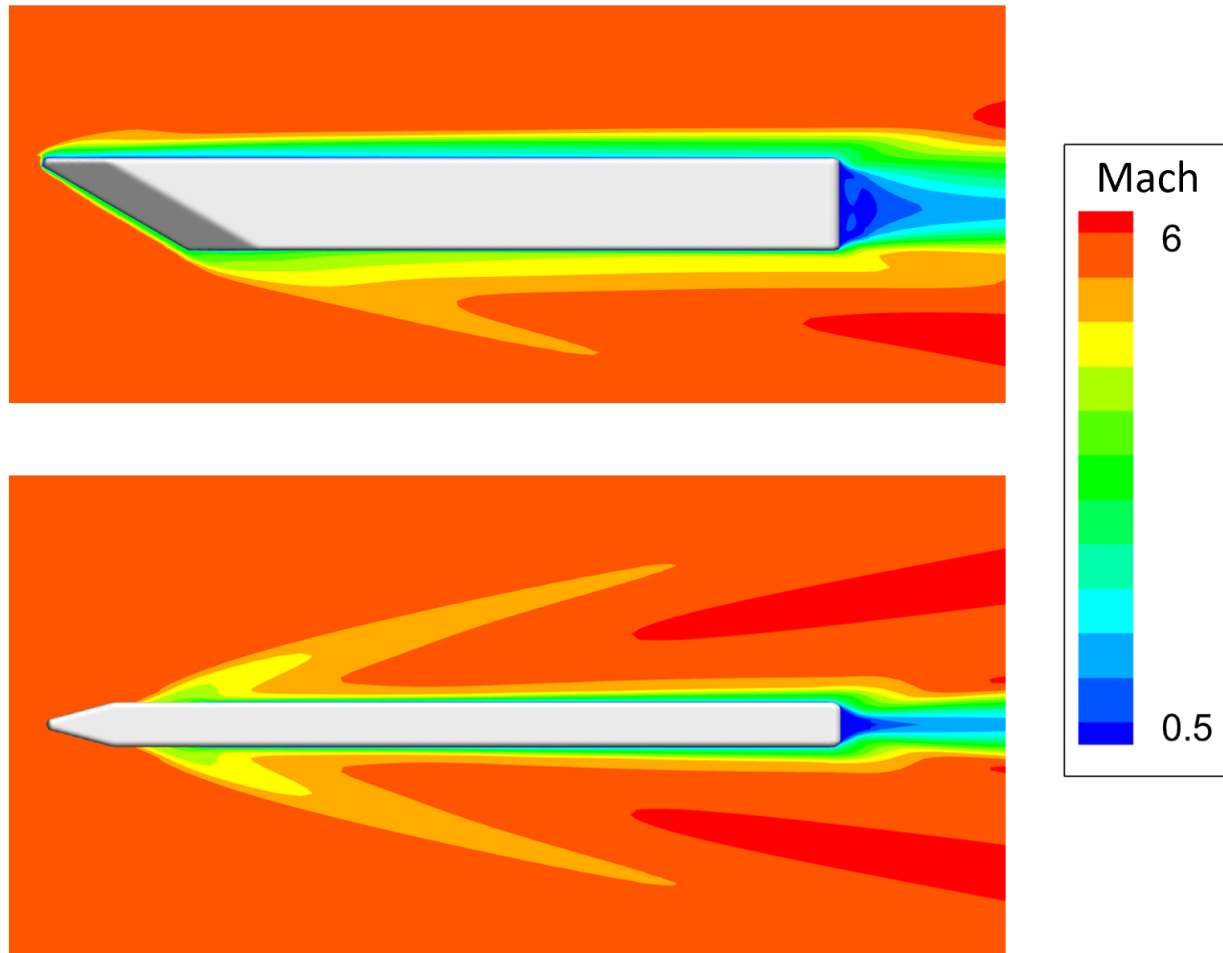


Figure 3-10: Mach contour slices from a 3D RANS CFD analysis performed on the probe geometry.

The slice in the lower plot is taken at the mid height of the probe head. Due to the swept leading edge, the shocks appear to be shifted downstream, but this is only an artifact of the slice location. The upper plot shows a much more significant flow disturbance off the lower surface of the probe than the upper surface.

The cooling scheme for the probe is illustrated in the cross section shown in Figure 3-11 which shows the cooling channels surrounding the internal cavity. The internal cavity provides room for the optics and associated fixtures as well as coupling hardware for the probe body. The channels are sized according to the relationship between width and aspect ratio found in section 3.1.2, which gives that the height should be near 1 cm, and the width should be longer than this to provide an internal temperature low enough to support the optics.

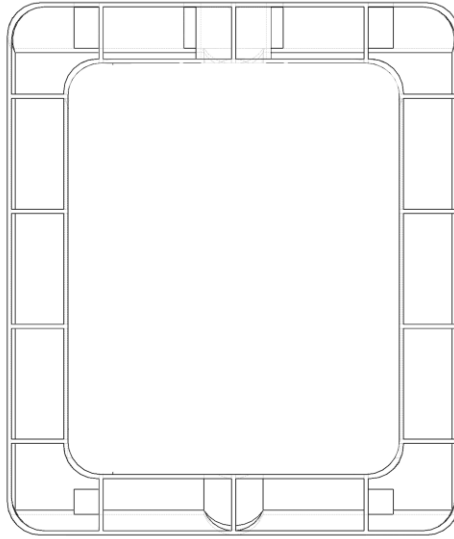


Figure 3-11: Cross section of the probe body showing the cooling channel geometry.

The coolant enters the cooling channels through a plenum integrated into the aft end of the probe and travels towards the leading edge. An array of small holes on the leading-edge faces allows the coolant to be exhausted and provide film cooling. This scheme is illustrated in a diagram in Figure 3-12.

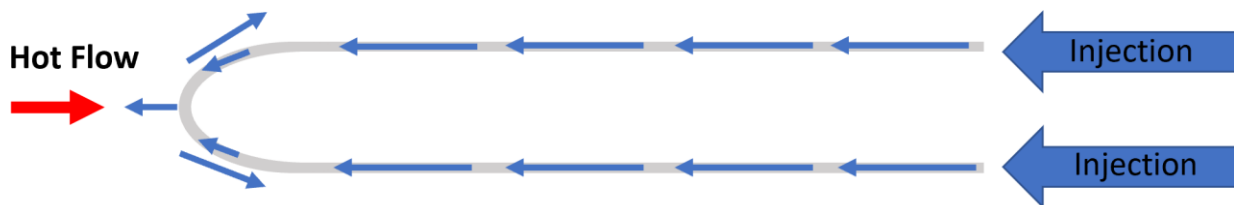


Figure 3-12: Diagram of open cycle coolant scheme.

The stem section of the probe has an independent set of coolant channels with the same cross section as those in the head section and an independent plenum and coolant inlet. The mechanical aspects of the assembly are discussed in the following section.

3.3 Proof of Concept Prototype

Validation of the cooling method and probe design will be conducted experimentally with a prototype that is much smaller than the full-scale probe but shares many fundamental design features. The prototype will only make room for one set of optics and, therefore, will be unable to host the requisite optics for FLASH MTV. Instead, FLEET MTV will be demonstrated. Figure 3-13 shows the prototype. The total length is significantly shorter than the full probe, and the height is 2" shorter.

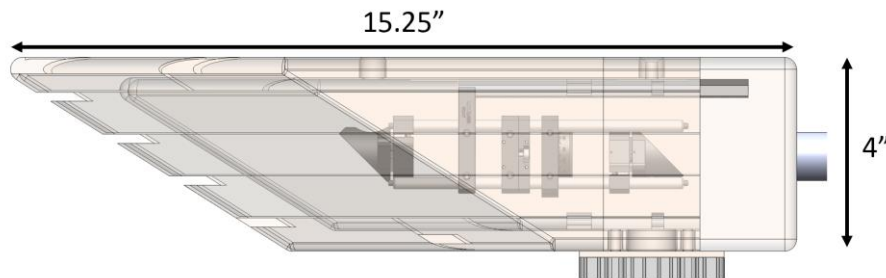


Figure 3-13: A transparent view of the probe prototype.

The probe assembly is designed to allow ease of interaction and installation of the optics. There are three primary sections, the leading section, which hosts most of the cooling channel length, the ejection holes, and the window, the mid-section, which hosts the laser entrance port and the mounting holes, and the aft section, which hosts the plenum and coolant inlet. Figure 3-14 shows the important mechanical aspects of the midsection, which is the root part of the probe. The three pieces are secured via screws which enter through dedicated channels in the aft section and thread into the leading section. A threaded hole on the leading section and a guide hole on the mid-section are visible in the probes bottom right internal corner in the figure. The bottom of the mid-section is also visible and shows the laser entry port surrounded by for mounting holes.

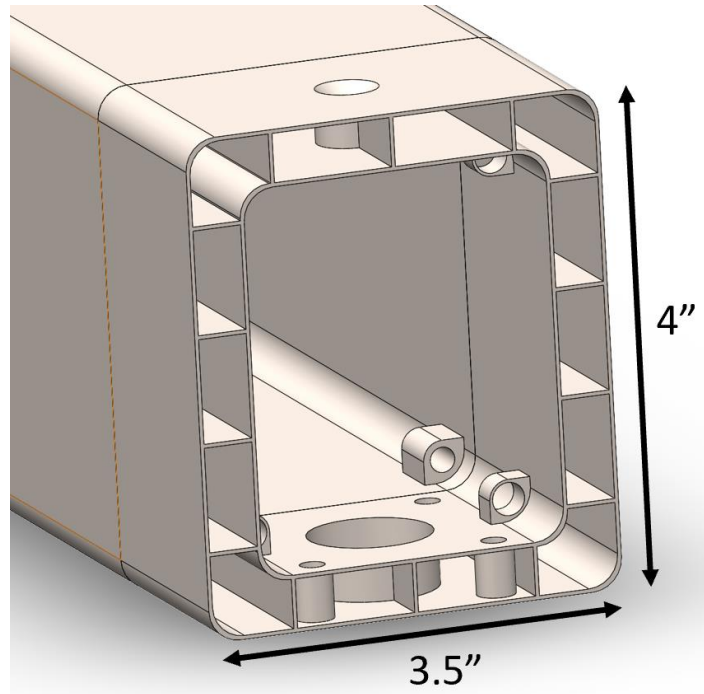


Figure 3-14: An image detailing the important mechanical aspects of the probe mid-section.

The countersunk hole visible on top of the mid-section is for securing the dovetail optical rail to the probe. This rail also serves to align the three parts which have a matching track.

The complex geometry of these parts, and the need for stainless steel (as shown in section 3.1.2), requires additive manufacturing techniques. An AM250 metal 3D printer will be used with 316L-0407 stainless steel powder to manufacture the parts.

Figure 3-15 shows a rendering of the prototype mounted on a test stand. A nitrogen line is shown coupled with the coolant port on the aft section. The plenum will make use of a deflection type design to assure evenly distributed coolant mass flow. The probe is mounted via the mid-section onto a stainless steel plate that is fixed to a stand made from t-slotted aluminum rails. The cooling performance will be evaluated in long duration tests with Zucrow Labs hot air supply. The aerodynamic performance in supersonic flow will be evaluated in short duration tests with the exhaust of the THOR RDE.

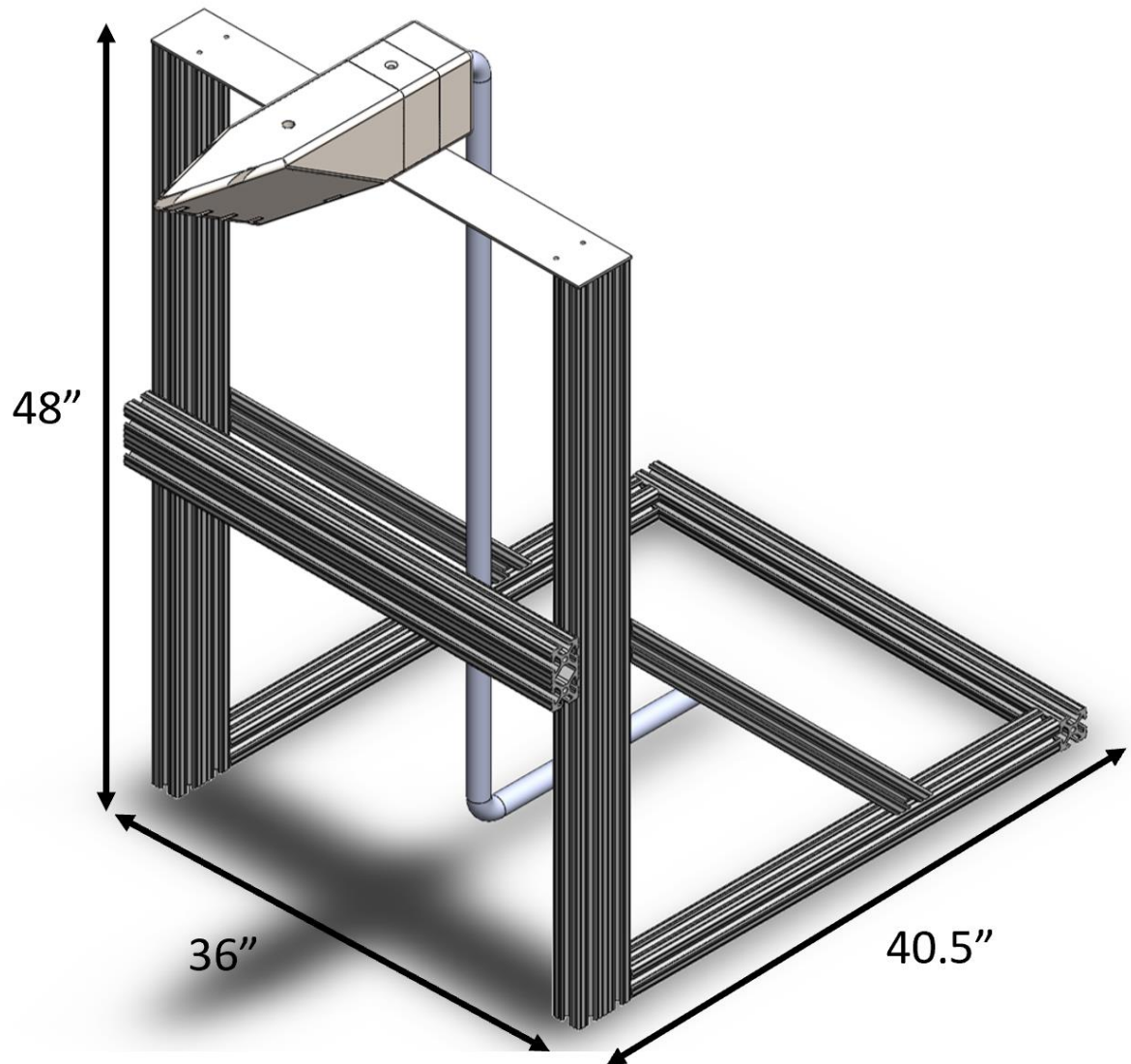


Figure 3-15: A CAD rendering of the prototype probe and test stand.

4. CONCLUSIONS

The objectives of this research were to first develop a force balance to apply precise and traceably accurate loads up to 400 pounds, with a precision less than or equal to 1%, enabling the calibration of thrust stands to precisions better than the cited 5% for the expected thrust range, and second to develop a cooled nacelle for optical components, such that laser velocimetry techniques can be performed within the core of high-temperature flows up to Mach 6 at total temps of 1700K.

The methodology for the first objective was successfully implemented. A novel use of hysteresis to quantify the friction and transmission factors for a pulley system allowed the precise determination of mechanical advantage provided by a block and tackle with friction. The block and tackle **produced loads up to 416 pounds** at an effort of 104.5 pounds. The designed t-slot rail construction allowed for disassembly, storage, reassembly, and mounting within a matter of hours. The root components of the system and model were also reconfigured to apply torques for torquemeter calibration applications. A notable limitation of the precision with which the applied load can be known is the friction method's dependence on the sensor's uncertainty; despite the unideal performance of the FUTEK loadcell, **maximum load uncertainties of 0.85%** were achieved. Much higher precisions are achievable with reductions in sensor, weight, and cable angle uncertainties, all of which are feasible. The system was finally used for a calibration of the Turbine High pressure Optical Accessible Rotating detonation combustor thrust stand.

The second methodology was accomplished by developing a script to iteratively solve for steady state equilibrium wall temperature for a finite fluid element and integrate along a 1-D coolant path to estimate cooling jacket performance. The cooling effectiveness of water, diluted glycol, and gaseous nitrogen were compared. Parametric studies using the 1-D analysis were performed on coolant type, coolant pressures, and channel geometries at Mach 6, 1,700 K, flow conditions. Gaseous nitrogen at 10 bar head with 1 cm tall cooling channels in an open cycle configuration and stainless-steel construction was selected to keep **internal temperatures below 40 degrees Celsius** and **external temperatures below 500 degrees Celsius** based on the parametric analysis. A 3-D Reynold's averaged Navier-Stokes simulation of the probe body was performed to assess flow perturbation and assure minimum disturbance in the measurement region. A mechanical design was developed for installation and operation of optical components. Finally, a prototype probe body was designed and will be tested at Zucrow labs.

REFERENCES

- [1] M. N. Nejaamtheen, J.-M. Kim and J.-Y. Choi, "Review on the Research Progresses in Rotating Detonation Engine," in *Detonation Control for Propulsion*, Springer, Cham, 2018, pp. 109-159.
- [2] E. T. Curran, "Scramjet Engines: The First Forty Years," *Journal of Propulsion and Power*, vol. 17, no. 6, pp. 1138-1148, 2001.
- [3] D. P. Stechmann, S. D. Heister and A. J. Harroun, "Rotating Detonation Engine Performance Model for Rocket Applications," *Journal of Spacecraft and Rockets*, vol. 56, no. 3, pp. 887-898, 2019.
- [4] Committee on Air Force and Department of Defense Aerospace Propulsion Needs, Air Force Studies Board, Division on Engineering and Physical Sciences, A REVIEW OF UNITED STATES AIR FORCE and DEPARTMENT OF DEFENSE Aerospace Propulsion Needs, Washington D.C.: The National Academies Press, 2006.
- [5] G. P. Sutton and O. Biblarz, *Rocket Propulsion Elements - Ninth Edition*, Hoboken: John Wiley & Sons, Inc., 2017.
- [6] A. Kawasaki, T. Inakawa, JiroKasahara, K. Goto, K. Matsuoka, A. Matsuo and I. Funaki, "Critical condition of inner cylinder radius for sustaining rotating detonation waves in rotating detonation engine thruster," *Proceedings of the Combustion Institute*, vol. 37, pp. 3461-3469, 2019.
- [7] B. A. Rankin, T. A. Kaemming, S. W. Theuerkauf and F. R. Schauer, "Overview of Performance, Application, and Analysis of Rotating Detonation Engine Technologies," *Journal of Propulsion and Power*, vol. 33, no. 1, pp. 131-143, 2017.
- [8] M. L. Fotia, T. A. Kaemming, J. Hoke, J. R. Codoni and F. Schauer, "Experimental Thrust Sensitivity of a Rotating Detonation Engine to Various Aerospike Plug-Nozzle Configurations," in *AIAA SciTech Forum*, San Diego, 2019.

- [9] R. Yokoo, K. Goto, J. Kim, A. Kawasaki, K. Matsuoka, J. Kasahara, A. Matsuo and I. Funaki, "Propulsion Performance of Cylindrical Rotating Detonation Engine," *AIAA Journal*, vol. 58, no. 12, pp. 5107-5116, 2020.
- [10] Ian V. Walters, R. M. Gejji, S. D. Heister and C. D. Slabaugh, "Flow and performance analysis of a natural gas-air rotating detonation engine with high-speed velocimetry," *Combustion and Flame*, vol. 232, 2021.
- [11] I. Dunn, J. Sosa, K. A. Ahmed, M. Salvadori and S. Menon, "Flowfield Velocity Measurements of a Rotating Detonation Engine," in *AIAA SciTech Forum*, Orlando, 2020.
- [12] J. Tobias, D. Depperschmidt, C. Welch, R. Miller, M. Uddi, A. K. Agrawa and J. Ron Daniel, "OH* Chemiluminescence Imaging of the Combustion Products From a Methane Fueled Rotating Detonation Engine," *Journal of Engineering for Gas Turbines and Power*, vol. 141, pp. 021021-1-11, 2019.
- [13] S. W. Theuerkauf, F. R. Schauer and R. Anthony, "Comparison of Simulated and Measured Instantaneous Heat Flux in a Rotating Detonation Engine," in *AIAA SciTech Forum*, San Diego, 2016.
- [14] S. J. Meyer, M. D. Polanka, F. R. Schauer and J. L. Hoke, "Parameter Impact on Heat Flux in a Rotating Detonation Engine," in *AIAA SciTech Forum*, Kissimmee, 2018.
- [15] J. Braun, J. Sousa and G. Paniagua, "Numerical Assessment of the Convective Heat Transfer in Rotating Detonation Combustors Using a Reduced-Order Model," *Applied Sciences*, vol. 8, no. 893, 2018.
- [16] J. R. E. Smith and S. Wehofer, "Measurement of Engine Thrust in Altitude Ground Test Facilities," in *AIAA 12th Aerodynamic Testing Conference*, Williamsburg, 1982.
- [17] V. Athmanathan, J. M. Fisher, Z. M. Ayers, D. G. Cuadrado, V. Andreoli, J. Braun, T. R. Meyer, G. Paniagua, C. A. Fugger and S. Roy, "Development of a turbine-integrated high-pressure optical RDE (THOR) for time-resolved fluid dynamic measurements using high-speed optical diagnostics," *AIAA Propulsion and Energy 2019 Forum*, p. 4041, 2019.
- [18] B. R. R. R. J. J. P and J. F. Seely, "Thrust Stand Design Principles," in *AIAA 17th Aerospace Ground Testing Conference*, Nashville, 1992.

- [19] A. Feleo, F. Chacon and M. Gamba, "Uncertainties in Thrust and EAP Measurements of a Rotating Detonation Combustor with Axial Air Inlet," in *AIAA Propulsion and Energy Forum*, 2020.
- [20] J. R. Mateos, "Design, implementation and calibration of a three-component Balance for a novel distributed propulsion concept," Valencia Polytechnic University, Valencia, 2014.
- [21] N. J. DELUCA, R. B. MILES, N. JIANG, W. D. KULATILAKA, A. K. PATNAIK and J. R. GORD, "FLEET velocimetry for combustion and flow diagnostics," *Applied Optics* vol. 56, no. 31, 2017.
- [22] J. M. Fisher, J. Braun, T. R. Meyer and G. Paniagua, "Application of femtosecond laser electronic excitation tagging (FLEET) velocimetry in a bladeless turbine," *Measurement Science and Technology* , vol. 31, no. 064005, 2020.
- [23] R. A. Burns and P. M. Danehy, "FLEET Velocimetry Measurements on a Transonic Airfoil," in *AIAA SciTech Forum*, Grapevine, 2017.
- [24] P. Viguier, J. Garraud, J.Soutade, L. Serre, S. Defoort, M. Ferrier and A. Ristori, "Development of F4 Hotshot Windtunnel for High Enthalpy Scramjet Tests," in *18th AIAA/3AF International Space Planes and Hypersonic Systems and Technologies Conference*, Tours, 2012.
- [25] L. SERRE, P. DENIS, N. CORTES and F. FALEMPIN, "DEVELOPMENT OF S4 FREE JET TEST FACILITY FOR THE FRENCH LEA FLIGHT TEST PROGRAM," in *17th AIAA International Space Planes and Hypersonic Systems and Technologies Conference*, San Francisco, 2011.
- [26] J.-F. Brouckaert, M. Mersinligil and M. Pau, "A Conceptual Design Study for a New High Temperature Fast Response Cooled Total Pressure Probe," *Journal of Engineering for Gas Turbines and Power*, vol. 131, no. 021602-2, 2009.
- [27] L. Bhatnagar, J. Braun, V. Andreoli, D. G. Cuadrado, Z. Liu and G. Paniagua, "DEVELOPMENTS IN HIGH FREQUENCY DIRECTIONAL PROBES FOR HIGH TEMPERATURE APPLICATIONS," in *XXIV Biennial Symposium on Measuring Techniques in Turbomachinery*, Prague, 2018.

- [28] M. Mersinligil, J. Desset and J. F. Brouckaert, "High-temperature high-frequency turbine exit flow field measurements in a military engine with a cooled unsteady total pressure probe," *Proc. IMechE*, vol. 225, pp. 954-963, 2011.
- [29] M. Miyasaka, J. Matheson, A. Lewis and B. Hannaford, "Measurement of the Cable-Pulley Coulomb and Viscous Friction for a Cable-Driven Surgical Robotic System," in *IEEE/RSJ International Conference on Intelligent Robots and Systems (IROS)*, Hamburg, 2015.
- [30] H. Olsson, K. .. Astrom, C. C. D. Wit, M. Gafvert and P. Lischinsky, "Friction models and friction compensation," *European journal of control*, vol 4, no. 3, pp. 176-195, 1998.
- [31] Y. Peng, Y. WEI and M. Zhou, "Efficient modeling of cable-pulley system with friction based on arbitrary-Lagrangian-Eulerian approach," *Applied Mathematics and Mechanics (English Edition)*, vol. 38, no. 12, pp. 1785-1802, 2017.
- [32] J. R. Taylor, *An Introduction to Error Analysis - The Study of Uncertainties in Physical Measurements*. Second Edition, University Science Books, 1997.
- [33] D. Cuadrado, P. A. N. Aye-Addo, V. Andreoli, L. Bhatnagar, F. Lozano, J. Fisher, G. Paniagua, J. Saavedra, D. Inman, T. Meyer, M. Bloxham, E. Clemens, B. Stults, T. White, A. Wallace and D. Johnson, "Purdue Small Turbine Aerothermal Rotating Rig (STARR)," in *AIAA Propulsion and Energy 2019 Forum*, Indianapolis, 2019.
- [34] S. D. Heister, W. E. Anderson, T. Pourpoint and R. J. Cassidy, *Rocket Propulsion*, Cambridge: Cambridge University Press, 2019.
- [35] Ames Aeronautical Laboratory, "Equations, Tables, and Charts for Compressible Flow," National Advisory Committee for Aeronautics, Moffett Field, 1953.
- [36] Y. A. Cengel, J. M. Cimbala and R. H. Turner, *Fundamentals of Thermal-Fluid Sciences - Fourth Edition*, New York: McGraw-Hill, 2012.
- [37] W. H. McAdams, *Heat Transmission - Second Edition*, New York: McGraw-Hill, 1942.
- [38] R. H. S. Winterton, "Where did the Dittus and Boelter equation come from?," *International Journal of Heat and Mass Transfer*, vol. 41, no. 4-5, pp. 809-810, 1998.